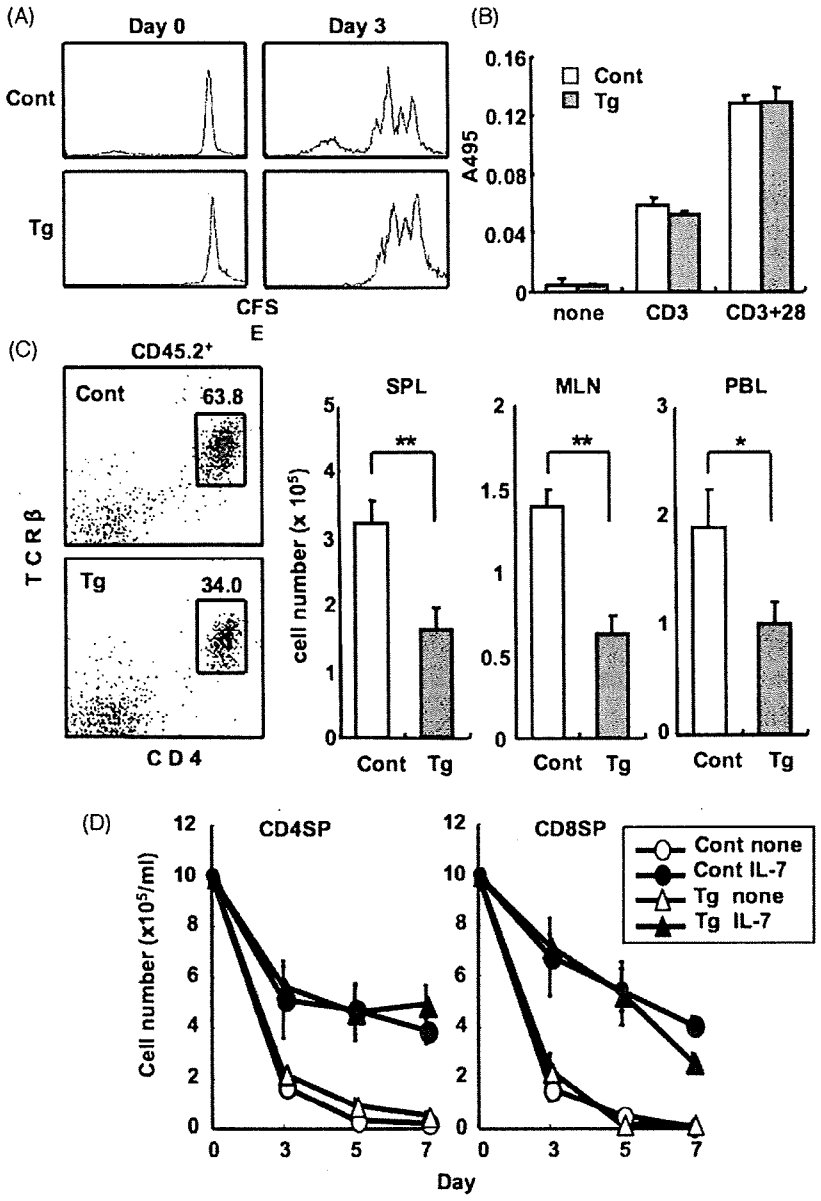

Fig. 7. Proliferation and survival of mature T cells in dnRac1-Tg mice. Splenic CD4-SP T cells were isolated from dnRac1-Tg mice (Tg) and littermate control mice (Cont). (A) CFSE-labeled CD4-SP T cells were stimulated with plate-bound anti-CD3 Ab, and cultured for 3 days. After incubation, cells were analyzed by flow cytometry. (B) After 3 days culture with stimulation, growth of CD4-SP T cells was evaluated by MTT method. (C) CD45.2$^+$CD4-SP T cells from dnRac1-Tg mice and littermate control mice were transferred into CD45.1$^+$RAG2$^{-/-}$ mice. After 40 days, CD45.2$^+$ CD4-SP T cells in spleen, mLN and PBL were analyzed. FACS data represent one of two similar experiments for each group in the spleen. Bar graphs of the number of CD45.2$^+$ CD4-SP cells were calculated on the basis of the percentages obtained by flow cytometry, and results are expressed as the mean ± S.E.M. of two independent experiments ($n = 10$). $^*p < 0.05$; $^{**}p < 0.01$. (D) Splenic CD4-SP and CD8-SP T cells were sorted and cultured with or without 1 ng/ml recombinant IL-7 up to 7 days in vitro. Live cells were counted after the indicated period.

[48], it is possible that migration defect would account for impaired T cell survival in vivo.

Collectively, Rac GTPases are important in survival of DP cells and also survival of mature T cells possibly by an Akt-dependent manner. Further analysis of the precise function of Rac in signal transduction of T cells will reveal the significance of Rac GTPases in T cell survival and development.

Acknowledgements

The authors thank Drs. A. Yuo, D. Chida, T. Dohi for technical instructions.

References

[1] Bustelo XR, Sauzeau V, Berenjeno IM. GTP-binding proteins of the Rho/Rac family: regulation, effectors and functions in vivo. Bioessays 2007;29:356–70.
[2] Cantrell DA. GTPases and T cell activation. Immunol Rev 2003;192:122–30.
[3] Scheele JS, Marks RE, Boss GR. Signaling by small GTPases in the immune system. Immunol Rev 2007;218:92–101.
[4] Van Aelst L, D'Souza-Schorey C. Rho GTPases and signaling networks. Genes Dev 1997;11:2295–322.
[5] Gu Y, Filippi MD, Cancelas JA, Siefring JE, Williams EP, Jasti AC, et al. Hematopoietic cell regulation by Rac1 and Rac2 guanosine triphosphatases. Science 2003;302:445–9.
[6] Brenner B, Koppenhoefer U, Weinstock C, Linderkamp O, Lang F, Gulbins E. Fas- or ceramide-induced apoptosis is mediated by a Rac1-regulated activation of Jun N-terminal kinase/p38 kinases and GADD153. J Biol Chem 1997;272:22173–81.

Please cite this article in press as: Sato Y, et al. Rac GTPases are involved in development, survival and homeostasis of T cells. Immunol Lett (2009), doi:10.1016/j.imlet.2009.03.014

[7] Hall A. Rho GTPases and the actin cytoskeleton. Science 1998;279:509–14.
[8] Arrieumerlou C, Randriamampita C, Bismuth G, Trautmann A. Rac is involved in early TCR signaling. J Immunol 2000;165:3182–9.
[9] Kim C, Dinauer MC. Rac2 is an essential regulator of neutrophil nicotinamide adenine dinucleotide phosphate oxidase activation in response to specific signaling pathways. J Immunol 2001;166:1223–32.
[10] Gomez JC, Soltys J, Okano K, Dinauer MC, Doerschuk CM. The role of Rac2 in regulating neutrophil production in the bone marrow and circulating neutrophil counts. Am J Pathol 2008;173:507–17.
[11] Arana E, Vehlow A, Harwood NE, Vigorito E, Henderson R, Turner M, et al. Activation of the small GTPase Rac2 via the B cell receptor regulates B cell adhesion and immunological-synapse formation. Immunity 2008;28:88–99.
[12] Corbetta S, D'Adamo P, Gualdoni S, Braschi C, Berardi N, de Curtis I. Hyperactivity and novelty-induced hyperreactivity in mice lacking Rac3. Behav Brain Res 2008;186:246–55.
[13] Sugihara K, Nakatsuji N, Nakamura K, Nakao K, Hashimoto R, Otani H, et al. Rac1 is required for the formation of three germ layers during gastrulation. Oncogene 1998;17:3427–33.
[14] Cancelas JA, Lee AW, Prabhakar R, Stringer KF, Zheng Y, Williams DA. Rac GTPases differentially integrate signals regulating hematopoietic stem cell localization. Nat Med 2005;11:886–91.
[15] Jansen M, Yang FC, Cancelas JA, Bailey JR, Williams DA. Rac2-deficient hematopoietic stem cells show defective interaction with the hematopoietic microenvironment and long-term engraftment failure. Stem Cells 2005;23:335–46.
[16] Walmsley MJ, Ooi SK, Reynolds LF, Smith SH, Ruf S, Mathiot A, et al. Critical roles for Rac1 and Rac2 GTPases in B cell development and signaling. Science 2003;302:459–62.
[17] Li B, Yu H, Zheng W, Voll R, Na S, Roberts AW, et al. Role of the guanosine triphosphatase Rac2 in T helper 1 cell differentiation. Science 2000;288:2219–22.
[18] Croker BA, Handman E, Hayball JD, Baldwin TM, Voigt V, Cluse LA, et al. Rac2-deficient mice display perturbed T-cell distribution and chemotaxis, but only minor abnormalities in T(H)1 responses. Immunol Cell Biol 2002;80:231–40.
[19] Yu H, Leitenberg D, Li B, Flavell RA. Deficiency of small GTPase Rac2 affects T cell activation. J Exp Med 2001;194:915–26.
[20] Gomez M, Tybulewicz V, Cantrell DA. Control of pre-T cell proliferation and differentiation by the GTPase Rac-I. Nat Immunol 2000;1:348–52.
[21] Gomez M, Kioussis D, Cantrell DA. The GTPase Rac-1 controls cell fate in the thymus by diverting thymocytes from positive to negative selection. Immunity 2001;15:703–13.
[22] Guo F, Cancelas JA, Hildeman D, Williams DA, Zheng Y. Rac GTPase isoforms, Rac1 and Rac2, play a redundant and crucial role in T-cell development. Blood 2008;112:1767–75.
[23] Dumont C, Corsoni-Tadrzak A, Ruf S, de Boer J, Williams A, Turner M, et al. Rac GTPases play critical roles in early T cell development. Blood 2009;113:3990–8.
[24] Hwang SY, Jung JW, Jeong JS, Kim YJ, Oh ES, Kim TH, et al. Dominant-negative Rac increases both inherent and ionizing radiation-induced cell migration in C6 rat glioma cells. Int J Cancer 2006;118:2056–63.
[25] Marinari B, Costanzo A, Viola A, Michel F, Mangino G, Acuto O, et al. Vav cooperates with CD28 to induce NF-kappaB activation via a pathway involving Rac-1 and mitogen-activated kinase kinase 1. Eur J Immunol 2002;32:447–56.
[26] Oda H, Suzuki H, Sakai K, Kitahara S, Patrick MS, Azuma Y, et al. Rac1-mediated Bcl-2 induction is critical in antigen-induced CD4 single-positive differentiation of a CD4+CD8+ immature thymocyte line. J Leukoc Biol 2007;81:500–8.
[27] Zhumabekov T, Corbella P, Tolaini M, Kioussis D. Improved version of a human CD2 minigene based vector for T cell-specific expression in transgenic mice. J Immunol Methods 1995;185:133–40.
[28] Bolis A, Corbetta S, Cioce A, de Curtis I. Differential distribution of Rac1 and Rac3 GTPases in the developing mouse brain: implications for a role of Rac3 in Purkinje cell differentiation. Eur J Neurosci 2003;18:2417–24.
[29] Melton E, Sarner N, Torkar M, van der Merwe PA, Russell JQ, Budd RC, et al. Transgene-encoded human CD2 acts in a dominant negative fashion to modify thymocyte selection signals in mice. Eur J Immunol 1996;26:2952–63.
[30] Mao C, Tili EG, Dose M, Haks MC, Bear SE, Maroulakou I, et al. Unequal contribution of Akt isoforms in the double-negative to double-positive thymocyte transition. J Immunol 2007;178:5443–53.
[31] Juntilla MM, Wofford JA, Birnbaum MJ, Rathmell JC, Koretzky GA. Akt1 and Akt2 are required for alphabeta thymocyte survival and differentiation. Proc Natl Acad Sci USA 2007;104:12105–10.
[32] Juntilla MM, Koretzky GA. Critical roles of the PI3K/Akt signaling pathway in T cell development. Immunol Lett 2008;116:104–10.
[33] Cunningham NR, Artim SC, Fornadel CM, Sellars MC, Edmonson SG, Scott G, et al. Immature CD4+CD8+ thymocytes and mature T cells regulate Nur77 distinctly in response to TCR stimulation. J Immunol 2006;177:6660–6.
[34] Swat W, Montgrain V, Doggett TA, Douangpanya J, Puri K, Vermi W, et al. Essential role of PI3Kdelta and PI3Kgamma in thymocyte survival. Blood 2006;107:2415–22.
[35] Azzam HS, Grinberg A, Lui K, Shen H, Shores EW, Love PE. CD5 expression is developmentally regulated by T cell receptor (TCR) signals and TCR avidity. J Exp Med 1998;188:2301–11.
[36] Alessi DR, Andjelkovic M, Caudwell B, Cron P, Morrice N, Cohen P, et al. Mechanism of activation of protein kinase B by insulin and IGF-1. EMBO J 1996;15:6541–51.
[37] Gold MR, Scheid MP, Santos L, Dang-Lawson M, Roth RA, Matsuuchi L, et al. The B cell antigen receptor activates the Akt (protein kinase B)/glycogen synthase kinase-3 signaling pathway via phosphatidylinositol 3-kinase. J Immunol 1999;163:1894–905.
[38] Franke TF, Yang SI, Chan TO, Datta K, Kazlauskas A, Morrison DK, et al. The protein kinase encoded by the Akt proto-oncogene is a target of the PDGF-activated phosphatidylinositol 3-kinase. Cell 1995;81:727–36.
[39] Burgering BM, Coffer PJ. Protein kinase B (c-Akt) in phosphatidylinositol-3-OH kinase signal transduction. Nature 1995;376:599–602.
[40] del Peso L, Gonzalez-Garcia M, Page C, Herrera R, Nunez G. Interleukin-3-induced phosphorylation of BAD through the protein kinase Akt. Science 1997;278:687–9.
[41] Reif K, Burgering BM, Cantrell DA. Phosphatidylinositol 3-kinase links the interleukin-2 receptor to protein kinase B and p70 S6 kinase. J Biol Chem 1997;272:14426–33.
[42] Genot EM, Arrieumerlou C, Ku G, Burgering BMT, Weiss A, Kramer IM. The T-cell receptor regulates Akt (protein kinase B) via a pathway involving Rac1 and phosphatidylinositide 3-kinase. Mol Cell Biol 2000;20:5469–78.
[43] Jameson SC. Maintaining the norm: T-cell homeostasis. Nat Rev Immunol 2002;2:547–56.
[44] Broers AEC, Posthumus-van Sluijs SJ, Spits H, van der Holt B, Lowenberg B, Braakman E, et al. Interleukin-7 improves T-cell recovery after experimental T-cell-depleted bone marrow transplantation in T-cell-deficient mice by strong expansion of recent thymic emigrants. Blood 2003;102:1534–40.
[45] Tan JT, Dudl E, LeRoy E, Murray R, Sprent J, Weinberg KI, et al. IL-7 is critical for homeostatic proliferation and survival of naive T cells. Proc Natl Acad Sci USA 2001;98:8732–7.
[46] Clarke SR, Rudensky AY. Survival and homeostatic proliferation of naive peripheral CD4+ T cells in the absence of self peptide:MHC complexes. J Immunol 2000;165:2458–64.
[47] Masse GX, Corcuff E, Decaluwe H, Bommhardt U, Lantz O, Buer J, et al. Gamma(c) cytokines provide multiple homeostatic signals to naive CD4(+) T cells. Eur J Immunol 2007;37:2606–16.
[48] Cinalli RM, Herman CE, Lew BO, Wieman HL, Thompson CB, Rathmell JC. T cell homeostasis requires G protein-coupled receptor-mediated access to trophic signals that promote growth and inhibit chemotaxis. Eur J Immunol 2005;35:786–95.

Please cite this article in press as: Sato Y, et al. Rac GTPases are involved in development, survival and homeostasis of T cells. Immunol Lett (2009), doi:10.1016/j.imlet.2009.03.014

RhoH Plays Critical Roles in FcεRI-Dependent Signal Transduction in Mast Cells[1]

Hiroyo Oda,* Manabu Fujimoto,† Michael S. Patrick,*‡ Dai Chida,* Yoshinori Sato,* Yoshinao Azuma,‡ Hiroki Aoki,§ Takaya Abe,¶ Harumi Suzuki,[2]* and Mutsunori Shirai‡

RhoH is an atypical small G protein with defective GTPase activity that is specifically expressed in hematopoietic lineage cells. RhoH has been implicated in regulation of several physiological processes including hematopoiesis, integrin activation, and T cell differentiation and activation. In the present study, we investigated the role of RhoH in mast cells by generating RhoH knockout mice. Despite observing normal development of mast cells in vivo, passive systemic anaphylaxis and histamine release were impaired in these mice. We also observed defective degranulation and cytokine production upon FcεRI ligation in RhoH-deficient bone marrow-derived mast cells. Furthermore, FcεRI-dependent activation of Syk and phosphorylation of its downstream targets, including LAT, SLP76, PLCγ1, and PLCγ2 were impaired, however phosphorylation of the γ-subunit of FcεRI remained intact. We also found RhoH-Syk association that was greatly enhanced by active Fyn. Our results indicate that RhoH regulates FcεRI signaling in mast cells by facilitating Syk activation, possibly as an adaptor molecule for Syk. ***The Journal of Immunology,*** **2009, 182: 957–962.**

RhoH is a newly identified hematopoietic small G protein, originally cloned as one of the genes frequently disrupted in diffuse large B cell lymphoma (1, 2). Because RhoH is defective in GTPase activity and thus constitutively active, the function of this protein was thought to be regulated by its expression level. Overexpression of RhoH inhibited RhoA/Rac/cdc42-dependent NF-κB activation in HEK293 cells (3), and it also inhibited SCF-mediated Rac1 activation in bone marrow progenitor cells (4). Knockdown of RhoH increased spontaneous LFA-1-mediated adhesion in Jurkat cells (5), and in vitro colony formation in bone marrow progenitor cells (4). Recent studies, however, have demonstrated that RhoH plays critical roles in T cell development (6, 7) by functioning as an adaptor for ZAP-70 in TCR signaling (7) via its tyrosine-phosphorylated ITAM-like motif (8). In the absence of RhoH, development of T cells in the thymus is impaired in both β-selection and positive selection, resulting in a severe reduction of mature peripheral T cells (6, 7). RhoH-deficient T cells showed defective phosphorylation of LAT and ERK upon TCR stimulation, indicating that RhoH is critical in TCR-dependent proximal signal transduction events. The precise function of RhoH in TCR signaling, however, remains controversial because there is a discrepancy in the phosphorylation status of ZAP-70 between two reports (6, 7). Furthermore, the physiological function of RhoH in other hematopoietic lineage cells is largely unknown.

Mast cells are widely distributed in the body and function as the primary effectors in immediate-type hypersensitivity reactions (9, 10). Mast cells recognize Ags via IgE and specific, high-affinity Fc receptors, termed FcεRI (11–13). FcεRI cross-linking triggers activation of Src family kinases Lyn and Fyn, and phosphorylation of ITAM motifs on the γ subunit of FcεRI complexes (14, 15). Subsequently, ZAP-70-related Syk kinase binds to phosphorylated ITAM motifs of the γ subunit and is thus activated by Src kinases (16–18). Activated Syk, in turn, phosphorylates LAT, LAT-2, and SLP-76 to form the signalosome, which transduces signals downstream, initiating Ca^{2+} mobilization, degranulation, and the expression of specific genes (19–21). The FcεRI-initiated signal cascade in mast cells is analogous to the TCR-initiated signal cascade in T cells, sharing many common molecules and features (14, 15, 22). This prompted us to investigate the function of RhoH in FcεRI signaling in mast cells.

In this study, we report the critical role of RhoH in mast cell activation. We established RhoH-deficient mice to unveil the physiological roles of RhoH in mast cells. RhoH-deficient mice showed impaired passive systemic anaphylaxis (PSA)[3] and histamine release upon challenge with the specific Ag. Our in vitro data showing impaired Syk activation with defective degranulation and cytokine production in $RhoH^{-/-}$ mast cells supports the observed in vivo phenotypes. Furthermore, we demonstrated that RhoH associates with Syk, and this interaction was greatly enhanced in the presence of constitutively active Fyn. These results suggest that RhoH acts as a positive regulator for FcεRI-mediated signal transduction by facilitating Syk activation.

*Department of Pathology, Research Institute, International Medical Center of Japan, Tokyo, Japan; †Department of Dermatology, Kanazawa University Graduate School of Medical Science, Kanazawa, Japan; ‡Department of Microbiology, Yamaguchi University School of Medicine, Ube, Japan; §Cardiovascular Research Institute Kurume University School of Medicine, Kurume, Japan; and ¶Laboratory for Animal Resources and Genetic Engineering, Center for Developmental Biology, RIKEN Kobe, Japan

Received for publication January 16, 2008. Accepted for publication November 6, 2008.

The costs of publication of this article were defrayed in part by the payment of page charges. This article must therefore be hereby marked *advertisement* in accordance with 18 U.S.C. Section 1734 solely to indicate this fact.

[1] This work was supported by grants from the Ministry of Education, Culture, Sports, Science and Technology.

[2] Address correspondence and reprint requests to Dr. Harumi Suzuki, Department of Pathology, Research Institute, International Medical Center of Japan, 1-21-1 Toyama, Shinjuku, Tokyo, Japan. E-mail address: hsuzuki@ri.imcj.go.jp

[3] Abbreviations used in this paper: PSA, passive systemic anaphylaxis; BMMC, bone marrow-derived mast cell; HSA, human serum albumin; HA, hemagglutinin.

Materials and Methods

Mice

RhoH knockout mice (Acc.No.CDB0483K) were generated using the previously described methods (23, 24). In brief, the entire ORF of the *RhoH* gene located in the third exon was replaced with a cassette consisting of a *lacZ* and *neomycin* resistance gene (*LacZ/neo*) by homologous recombination. The lengths of the homologous regions in the targeting vector were 8.2 kb and 4.8 kb at the 5′ and 3′ sides of the DT-A/LacZ/neo cassette (http://www.cdb.riken.jp/arg/cassette.html), respectively. Two mutant mouse lines were established from two independent homologous recombinant ES cell lines; no difference was found in their phenotype. All mice were maintained after five generations of backcrossing to C57BL/6J (B6) and housed under specific pathogen-free conditions in accordance with institutional guidelines.

Mast cell culture

Bone marrow-derived mast cells (BMMCs) were prepared as described (25). In brief, femurs were isolated from 8- to 20-wk-old RhoH$^{-/+}$ and RhoH$^{-/-}$ mice, and BM cells were cultured in 2% conditioned RPMI 1640 medium from X63-IL-3 cells (gift from Dr. H. Karasuyama, Tokyo Medical and Dental University, Tokyo, Japan), containing 10% heat-inactivated FBS. After at least 4 wk of culture, cells were stained with PE-conjugated anti-FcεRI Ab and allophycocyanin-conjugated anti-c-*kit* Ab (BD Biosciences) and their expression was confirmed before use in all experiments.

Plasmids

Hemagglutinin (HA)-tagged RhoH cDNA was cloned into pcDNA3 vector using a PCR-based strategy from a mouse thymus cDNA library made in our laboratory. Myc-tagged Syk and active type Fyn cloned in pcDNA3 vector were kind from Dr. T. Kurosaki (RIKEN Research Center for Allergy and Immunology, Yokohama, Japan) and Dr. T. Yamamoto (Institute of Medical Science, University of Tokyo, Tokyo, Japan).

Passive systemic anaphylaxis

Mouse IgE anti-DNP (100 μg, clone SPE-7, Sigma-Aldrich) was administered i.v. through the tail vein in volumes of 300 μl/mouse. After 24 h, 100 μg of DNP-human serum albumin (HSA) in 300 μl of PBS was injected i.v. Immediately after Ag challenge, body temperature was measured every 5 min by rectal thermometer. At 30 min following Ag challenge, mice were sacrificed and peripheral blood was taken by cardiac puncture and plasma was used for histamine enzyme immunoassay (SPI-BIO).

Degranulation assay

BMMCs (5×10^4 per well) on 96-well plates were sensitized with 1 μg/ml IgE anti-DNP for 4 h at 37°C. Next, cells were washed three times with Tyrode's Buffer (130 mM NaCl, 5 mM KCl, 1.4 mM $CaCl_2$, 1 mM $MgCl_2$, 5.6 mM glucose, 0.1% BSA, 10 mM HEPES (pH 7.4)) and stimulated for 30 min with the indicated concentration of DNP-HSA or A23187 (200 ng/ml, Sigma-Aldrich) in 100 μl of Tyrode's buffer. Samples were centrifuged and supernatant was collected to measure the released β-hexosaminidase. To determine the total cell content of this enzyme, the cell pellet was lysed with 0.5% Triton X-100 in Tyrode's buffer and the lysate was collected. For each sample, 50 μl of substrate solution (1.3 mg/ml 4-nitrophenyl N-acetyl-β-D-glucosaminide in 0.1 M sodium citrate (pH 4.5); Sigma-Aldrich) was added and incubated for 1 h at 37°C. The reaction was stopped by the addition of 150 μl of 0.2 M glycine solution (pH 10.7). The absorbance at 405 nm was measured in a microplate reader (Bio-Rad).

Calcium flux assay

BMMCs were sensitized with 1 μg/ml IgE anti-DNP at 10^6/ml without IL-3 and labeled with 3 μM of Fura2-AM (Invitrogen) for 30 min at 37°C. Then, cells were washed three times and resuspended in Tyrode's buffer at 5×10^5/ml. Fluorescence intensities were measured at an excitation wavelength of 340 or 380 nm and an emission wavelength of 510 nm, with a fluorescence spectrometer (Hitachi F-2500) during stimulation as indicated in Fig. 5.

Real-time RT-PCR analysis

Total RNA was isolated from 10^6 stimulated or nonstimulated BMMCs (as described above) using RNeasy kit (Qiagen), and cDNA was generated using the SuperScript III kit (Invitrogen) according to the manufacturer's instructions. Real-time PCR was conducted using the Platinum SYBR Green qPCR Supermix (Invitrogen) with specific primers for RhoH (5′gatcaggagcaacctacc ct3′/5′atgcaggaagccctgtga3′), IL-6 (5′gctaccaaactggatataatcagga3′/5′ccaggtag ctatggtactccagaa3′), TNF-α (5′tcttctcattcctgcttgtgg3′/5′ggtctgggccatagaactga 3′), and β-actin (5′aaggccaaccgtgaaaagat3′/5′gtggtacgaccagaggcatac3′).

Immunoblotting and immunoprecipitation

For immunoblotting, BMMCs were sensitized with 1 μg/ml anti-DNP IgE at 10^6 cells/ml for 4 h without IL-3, washed three times, and then stimulated with DNP-HSA for the indicated periods. Stimulated BMMCs were lysed in lysis/wash buffer (1% Nonidet P-40, 150 mM NaCl, 50 mM Tris-Cl (pH 8.0), 1 mM sodium orthovanadate, 1 mM DTT, proteinase inhibitors), subjected to 7.5–12.5% SDS-PAGE and Western blotting (10^5 cells per lane). For FcRγ and Lyn, 10^6 BMMCs were lysed with lysis/wash buffer and immunoprecipitated with 1 μg of the indicated Abs, then subjected to 12.5% SDS-PAGE in tricine-SDS running buffer (0.1 M Tris, 0.1 M Tricine, 0.1% SDS for the upper chamber, 0.2 M Tris-Cl (pH 8.9) for the lower chamber), and Western blotting. For RhoH and Syk, 4.5×10^5 293T cells were transiently transfected with HA-tagged RhoH, myc-tagged Syk with or without constitutively active Fyn using FuGENE 6 (Roche). After 24 h, transfected cells were incubated with or without 30 μM PP2 (src kinase inhibitor) for 2 h before lysis. After 2 h, cells were lysed with magnesium containing lysis/wash buffer (1% NP40, 10 mM $MgCl_2$, 25 mM HEPES (pH 7.3), 150 mM NaCl, 8% glycerol, 1 mM EDTA, 1 mM sodium orthovanadate, and protease inhibitors), immunoprecipitated with 1 μg of the indicated Abs and then subjected to 12.5% SDS-PAGE in tricine-SDS running buffer. We confirmed that 30 μM of PP2 did not affect the overall tyrosine phosphorylation status of the cells, indicating that this concentration of PP2 specifically inhibits src kinases. Abs used for Western blotting and immunoprecipitation were anti-phospho Syk, -phospho PLCγ1, -phospho PLCγ2, -ERK, -phospho p38, -p38, -Lyn (Cell Signaling Technology), anti-phospho SLP76 and -phospho LAT (BD Biosciences), anti-phospho tyrosine (clone pY20, Neomarkers), anti-phospho tyrosine (clone 4G10), -myc and -HA (Roche) and -FcRγ (Millipore). We could not detect endogenous RhoH using commercially available or in-house generated RhoH Abs from rabbit or rat.

Histochemistry

To observe tissue mast cells, 6-μm paraffin sections of fixed tissues were stained with toluidine blue (Sigma-Aldrich) and the total number of mast cells in each tissue unit was counted. A skin unit was defined as the entire area of an ear section along the cartilage, and a stomach unit was defined as the entire area of a sagittal section.

Results

Generation of RhoH$^{-/-}$ mice

Mice carrying a mutant *RhoH* allele were generated from TT2 embryonic stem cells in which homologous recombination was used to replace the entire coding region located in exon 3 of the *RhoH* gene. As a result, there is no possibility of expression of any truncated forms of the protein in the mice (Fig. 1*A*). Offspring carrying the mutant allele were identified by Southern blotting (Fig. 1*B*). Homozygous *RhoH*-null mice were born at the expected Mendelian ratio.

Impaired FcεRI-mediated anaphylaxis in RhoH$^{-/-}$ mice

We found that RhoH is expressed in mast cells as well as T and B cells (Fig. 1*C*), as previously reported (4). Because the role of RhoH in immune cells other than T cells has not been characterized, we focused on mast cells in the present study. One of the major functions of mast cells is inducing allergy and anaphylaxis, therefore, we examined PSA, in which exogenously administered IgE is passively taken up by mast cells and degranulation is evoked by subsequent administration of Ag. As shown in Fig. 2*A*, the IgE-dependent PSA response in RhoH$^{-/-}$ mice, evaluated by the reduction of core body temperature after DNP-HSA injection, was smaller compared with those in RhoH$^{+/+}$ mice. As shown in Fig. 2*B*, measurement of plasma histamine concentration 30 min after DNP-HSA challenge revealed reduced secretion of histamine in RhoH$^{-/-}$ mice compared with RhoH$^{+/+}$ mice. Collectively, we demonstrated that RhoH is important in the systemic anaphylaxis reaction in vivo.

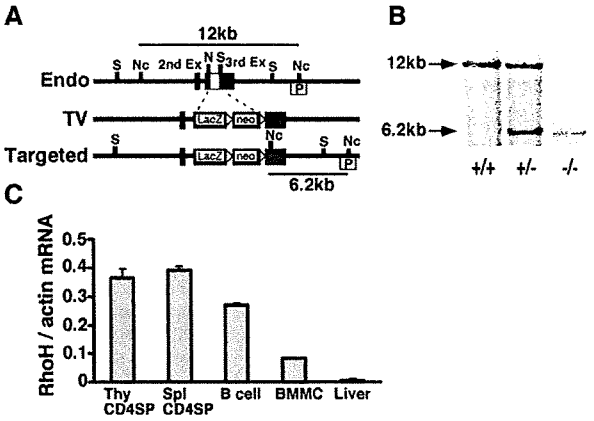

FIGURE 1. Generation of RhoH$^{-/-}$ mice. *A*, Targeting vector was designed to disrupt the *RhoH* gene by homologous recombination. The endogenous locus of *RhoH* (Endo), targeting vector (TV), and targeted locus (Targeted) are shown. The open box in the third exon represents the entire ORF of *RhoH* that was replaced by a *LacZ/neomycin* resistance gene. Restriction sites are abbreviated as follows: S, *SalI*; Nc, *NcoI*; N, *NotI*. P in the open box indicates the location of probe for Southern blotting. *B*, Southern blot analysis of *NcoI* digested mouse genomic DNA. A 12- and 6.2-kb band represent the wild-type and targeted alleles, respectively. *C*, Expression of RhoH mRNA was detected by real time RT-PCR in the indicated cells and tissues. Results are the mean and SE from three independent experiments, $n = 9$ for each group.

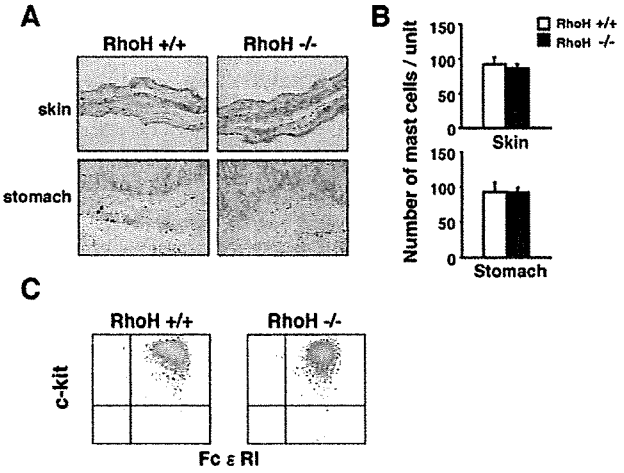

FIGURE 3. Normal development of mast cells in RhoH$^{-/-}$ mice. *A*, Mast cells in the ear skin (*upper*) and stomach (*lower*) in RhoH$^{+/+}$ and RhoH$^{-/-}$ mice were detected with toluidine blue staining. The highly metachromatic cells are mast cells. *B*, Number of mast cells in indicated tissues. Results are the mean and SE of mast cells per unit from indicated number of mice. For ear skin, $n = 4$ mice per group; for stomach, $n = 3$ per group. *C*, Expression of FcεRI and c-*kit* on the surface of BMMCs induced from RhoH$^{+/+}$ and RhoH$^{-/-}$ mice was analyzed by flow cytometry. Shown are representative data from more than five independent experiments.

Normal development of mast cells in RhoH$^{-/-}$ mice

Because we found impaired anaphylaxis in RhoH-deficient mice, we assessed the effect of RhoH disruption on mast cell development in vivo. Histological analysis by toluidine blue staining demonstrated that the anatomical distribution and morphology of connective tissue mast cells in the skin and mucosal mast cells in the stomach of RhoH$^{-/-}$ mice were comparable to those of RhoH$^{+/+}$ mice (Fig. 3*A*). The number of mast cells detected per area in these tissues was not changed in these mice (Fig. 3*B*). Growth rate and total number of in vitro induced BMMCs from RhoH-deficient mice were comparable to those from RhoH$^{+/+}$ mice (data not shown). After 4 wk culture, the proportion of FcεRI and c-*kit* double positive cells was >95% in both RhoH$^{-/-}$ and RhoH$^{+/+}$ BMMCs (Fig. 3*C*). From these results, we conclude that RhoH is dispensable for mast cell development both in vivo and in vitro.

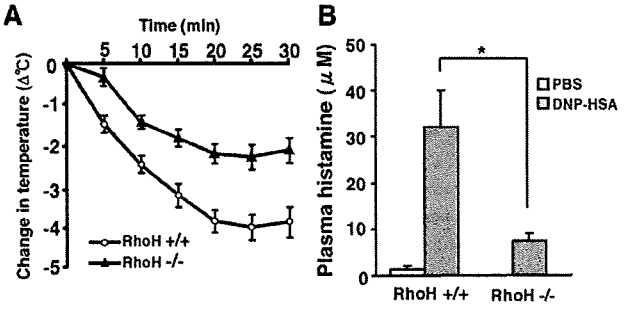

FIGURE 2. Impaired systemic anaphylaxis in RhoH$^{-/-}$ mice. *A*, RhoH$^{-/+}$ (○) and RhoH$^{-/-}$ (▲) mice were sensitized with anti-DNP IgE overnight, then challenged with DNP-HSA (100 μg), and the core body temperature was measured up to 30 min. Representative data of three independent experiments is shown. *B*, At 30 min after induction of PSA, peripheral blood was taken from RhoH$^{+/+}$ and RhoH$^{-/-}$ mice by cardiac puncture and the plasma histamine concentration was measured by EIA. Results are the mean and SE from three independent experiments. Statistical significance was determined by Welch's *t* test; *, $p < 0.05$. $n = 5$ control mice, $n = 6$ knockout mice.

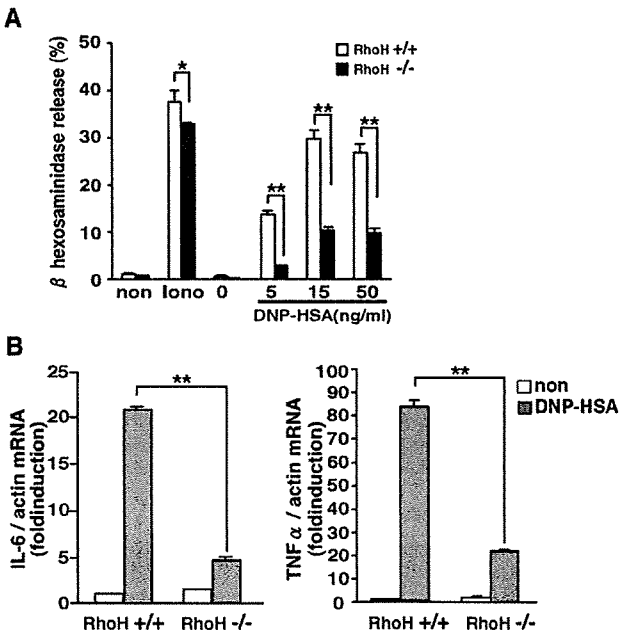

FIGURE 4. FcεRI-stimulated degranulation and cytokine production were impaired in RhoH$^{-/-}$ mast cells. *A*, BMMCs from RhoH$^{+/+}$ (□) and RhoH$^{-/-}$ (■) were sensitized with anti-DNP IgE, then 30 min after DNP-HSA (at the indicated concentrations) or A23187 (Iono, 200 ng/ml) stimulation, degranulation was assayed by β-hexosaminidase release. *B*, Anti-DNP IgE-sensitized BMMCs were stimulated with DNP-HSA (10 ng/ml) for 1 h or unstimulated. Then, IL-6 (*left*) and TNF-α (*right*) mRNA were quantified by real time RT-PCR. Results are the mean and SE from three independent experiments; $n = 9$ for each group. Statistical significance was determined by Student's *t* test; *, $p < 0.05$; **, $p < 0.01$.

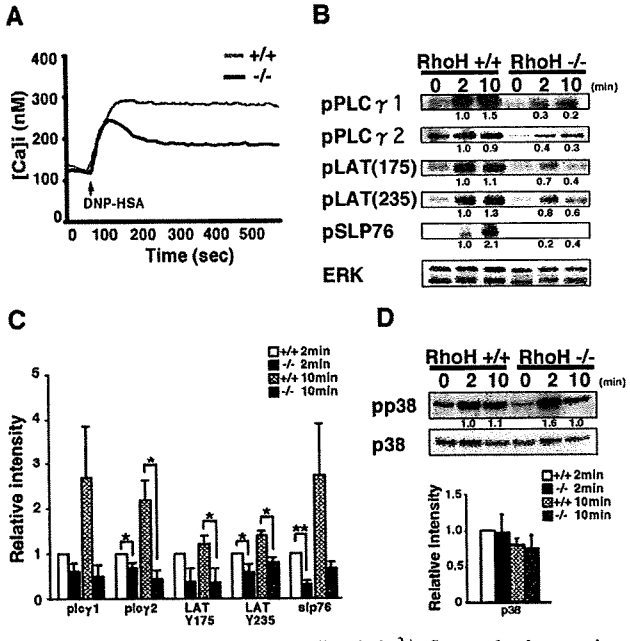

FIGURE 5. Defective FcεRI-mediated Ca^{2+} flux and adaptor phosphorylation in $RhoH^{-/-}$ mast cells. *A*, Ca^{2+} flux in $RhoH^{+/+}$ (gray line) and $RhoH^{-/-}$ (black line) BMMCs was monitored. Anti-DNP IgE sensitized BMMCs were stimulated with 100 ng/ml DNP-HSA at 70 s. Shown is representative data from two independent experiments, $n = 6$ for each group. *B*, Anti-DNP IgE sensitized BMMCs were stimulated with 10 ng/ml DNP-HSA for the indicated periods. Cell lysates were analyzed by Western blot using the indicated Abs. Numbers below the bands indicate the relative intensity of each band. Blotting for ERK was used for confirmation of equal loading to wells. Data shown is representation of three independent experiments. *C*, The bar graph represents band intensities from (*B*) relative to 2 min stimulated $RhoH^{+/+}$ in each lane. *D*, Activation of p38 in $RhoH^{-/-}$ BMMCs (*upper*). Shown is representative data from at least three independent experiments. Relative intensity of each sample is shown as in *C* (*lower*) with the mean and SE for the bar graph. Statistical significance was determined by paired *t* test; *, $p < 0.05$; **, $p < 0.01$.

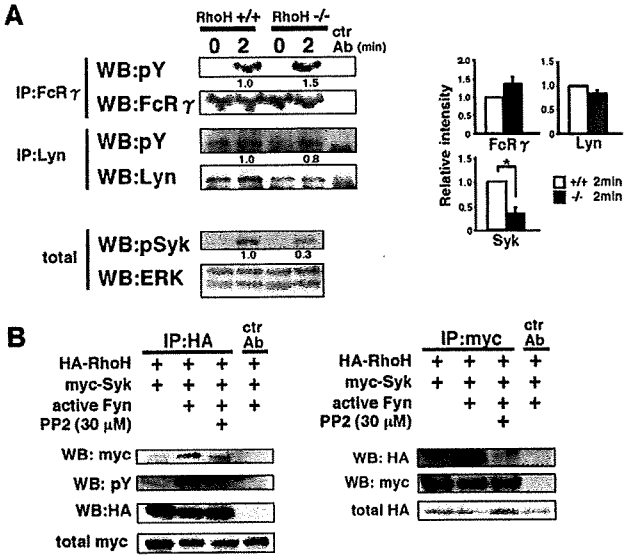

FIGURE 6. RhoH associates with Syk and regulates its activation. *A*, Anti-DNP IgE sensitized BMMCs were stimulated with 5 μg/ml anti-FcεRI for the indicated periods. Cell lysates were immunoprecipitated with anti-FcRγ Ab (*left upper*) or -Lyn Ab (*left middle*) or control Abs (ctr Ab) and analyzed by Western blotting using indicated Abs. The total lysates were analyzed by Western blotting using anti-phosphoSyk and -ERK Abs (*left lower*). The relative intensity to 2 min stimulated $RhoH^{+/+}$ BMMCs in each lane is shown in the right panel. Shown is representative data from three independent experiments and the mean and SE in the bar graph. Statistical significance was determined by paired *t* test; *, $p < 0.05$. *B*, 293T cells were transiently transfected with the indicated expression vectors. After 24 h, cells were incubated with or without PP2, lysed, and immunoprecipitated with anti-HA (*left*) or anti-myc (*right*) or control Abs (ctr Ab) followed by Western blotting with the indicated Abs. Total lysates were analyzed by Western blotting using anti-myc (*left*) or anti-HA Ab (*right*) to confirm the expression of myc-Syk or HA-RhoH, respectively.

FcεRI-mediated degranulation and cytokine production by $RhoH^{-/-}$ mast cells

The reduction in PSA without obvious developmental defects of mast cells in $RhoH^{-/-}$ mice indicated a functional deficiency in $RhoH^{-/-}$ mast cells. Therefore, we analyzed FcεRI-mediated degranulation of BMMCs from $RhoH^{-/-}$ mice in vitro. BMMCs were stimulated with varying doses of Ag, and degranulation was measured by the release of β-hexosaminidase, an enzyme found in mast cell granules. As shown in Fig. 4*A*, degranulation of RhoH-deficient BMMCs in response to Ag/IgE Ab-mediated cross-linking was significantly reduced.

Total β-hexosaminidase content from $RhoH^{+/+}$ and $RhoH^{-/-}$ BMMCs were comparable (data not shown), suggesting that RhoH is dispensable for granule biogenesis in BMMCs. We next measured gene expression of IL-6 and TNF-α (26), well-established targets of FcεRI signaling in mast cells. We stimulated $RhoH^{+/+}$ and $RhoH^{-/-}$ BMMCs for 1 h and then measured mRNA expression levels of IL-6 and TNF-α by real time RT-PCR. Expression of IL-6 and TNF-α in BMMCs was severely inhibited in the absence of RhoH (Fig. 4*B*).

Impaired Ca^{2+} influx and adapter phosphorylation in $RhoH^{-/-}$ mast cells

Engagement of FcεRI results in tyrosine phosphorylation of kinases and adaptors, and then an increase in intracellular Ca^{2+} concentration (27, 28). To explore the role of RhoH in FcεRI-dependent signal transduction, we first analyzed Ca^{2+} mobilization in RhoH-deficient BMMCs. As shown in Fig. 5*A*, Ca^{2+} concentration reached the maximum level within 150 s in cells from $RhoH^{+/+}$ and $RhoH^{-/-}$ mice after Ag challenge. The maximal Ca^{2+} concentration after the Ag challenge was, however, far less in RhoH-deficient BMMCs, indicating that the signaling defect in $RhoH^{-/-}$ cells lies upstream of Ca^{2+} mobilization. Indeed, phosphorylation of PLCγ1 and PLCγ2, which is essential for FcεRI-dependent Ca^{2+} mobilization, was significantly reduced in $RhoH^{-/-}$ BMMCs (Fig. 5, *B* and *C*). Because phosphorylation of the LAT adaptor is required for the activation of PLCγ1 and 2, we next investigated the phosphorylation status of LAT and SLP76 upon stimulation. As shown in Fig. 5, *B* and *C*, FcεRI-induced phosphorylation of both LAT (Y175 and Y235) and SLP76 were significantly inhibited. Conversely, the activation of p38 upon FcεRI engagement in RhoH BMMCs was comparable to that of $RhoH^{+/+}$ BMMCs (Fig. 5*D*).

RhoH associates with Syk and regulates its activation

These results imply the signal transduction upstream of these adaptors is defective in RhoH-deficient mast cells. The adaptors LAT and SLP-76 are phosphorylated by the kinase Syk upon antigenic stimulation (29), therefore we next examined the activation of Syk. We found that stimulation-dependent phosphorylation of Tyr 519/520 residues of Syk, a known determinant of its kinase activity, was severely reduced in RhoH-deficient BMMCs (Fig. 6*A*).

Therefore, we conclude that FcεRI-induced activation of Syk is dependent on RhoH, which is essential for the phosphorylation of LAT and SLP-76 adaptors as well as PLC phosphorylation and Ca^{2+} mobilization in mast cells.

Syk binds to phosphorylated tyrosines in the ITAM motif of the γ-subunit of FcεRI, and is phosphorylated by Lyn or by itself. We therefore examined phosphorylation of FcRγ and Lyn, which are the earliest events after FcεRI engagement and required for mast cells activation (30). As shown in Fig. 6*A*, phosphorylation of FcRγ and Lyn in $RhoH^{-/-}$ BMMCs was comparable to that in $RhoH^{+/+}$. These results indicate that cross-linking and activation of immediate downstream molecules of FcεRI occur normally in the absence of RhoH, and we concluded that the impaired phosphorylation of Syk is responsible for the defective FcεRI-dependent signal transduction in $RhoH^{-/-}$ BMMCs.

RhoH has been reported to associate with ZAP-70 in T cells (7). Because Syk and ZAP-70 belong to the same family and are functionally analogous, we hypothesized that RhoH might associate with Syk and act as an adaptor for Syk. To test this hypothesis, we coexpressed HA-tagged RhoH, myc-tagged Syk, and constitutively active Fyn in 293T cells and performed coimmunoprecipitation of RhoH and Syk. We found that RhoH associated with Syk and this association was enhanced by constitutively active Fyn (Fig. 6*B*). Concomitantly, RhoH was phosphorylated in the presence of active Fyn. Treatment of cells with PP2, an inhibitor of src family kinases, inhibited the phosphorylation of RhoH and the interaction between RhoH and Syk. Because FcεRI ligation activates Fyn in mast cells, RhoH would be able to interact with Syk more strongly, and therefore RhoH may function as an adaptor molecule for Syk in mast cells in a way analogous to that in T cells. This possibility may provide an explanation for the defective FcεRI signaling in $RhoH^{-/-}$ mast cells.

Discussion

Mast cells play important roles in initial immunological responses as well as in the clearance of parasitic infections (9, 10, 31, 32). One of the major functions of mast cells is the immediate release of histamine and other inflammatory mediators from their intracellular granules to increase vascular permeability upon antigenic cross-linking of surface FcεRI (33). In the present study, we demonstrated that the hematopoietic lineage specific atypical small GTPase RhoH, plays critical roles in mast cell function by facilitating phosphorylation of Syk in FcεRI-dependent signal transduction.

We observed impaired degranulation and cytokine production in RhoH deficient mast cells (Fig. 4) without obvious developmental defects of mast cells (Fig. 3). This result is consistent with the fact that FcεRI-dependent signaling is not required for mast cell development. As a matter of fact, the mast cell-related phenotype in $RhoH^{-/-}$ mice is similar to the one in mice deficient for Syk (16), LAT (34), SLP76 (35, 36), Fyn (18), or Btk (37, 38), which are all involved in FcεRI-related signaling. We observed both impaired Ca^{2+} influx and phosphorylation of PLCγ1 and 2, LAT (Y175, Y235), and SLP-76 (Y128) upon FcεRI stimulation in mast cells (Fig. 5). We saw a slight but reproducible decrease in ionomycin -induced degranulation in $RhoH^{-/-}$ BMMCs (Fig. 4*A*). Interestingly, a similar phenotype was seen in SLP76 mutant BMMCs, in which the calcium influx upon ionomycin treatment was lower than that of wild-type BMMCs (36). This might be because adaptor molecules like RhoH and SLP76 can affect the signaling events downstream of calcium release from the ER, or might indicate the existence for a possible positive feedback pathway from calcium signaling to the upstream of adaptor molecules.

RhoH was initially reported as an antagonist for the Rac1/RhoA/cdc42-dependent activation of NF-κB and p38 (3, 4), and has also been proposed to repress LFA-1 activation (5). More recently, RhoH has been reported to act as an adaptor for ZAP-70 by associating with ZAP-70 via its ITAM-like motif, and its association is enhanced upon TCR stimulation (7). ZAP-70 is not expressed in mast cells, but instead, Syk, which belongs to the same kinase family as ZAP-70, is expressed and plays essential roles in FcεRI signaling (16). In this study, we demonstrated that RhoH associates with Syk, and phosphorylated RhoH can interact with Syk more efficiently (Fig. 6*B*). Indeed, the reduced number of DP thymocytes in $RhoH^{-/-}$ mice cannot be explained by the functional defect of ZAP-70, because $ZAP\text{-}70^{-/-}$ mice showed normal β-selection (39). However, it is known that Syk and ZAP-70 have redundant roles in β-selection during T cell development (40). Therefore, our results showing that RhoH associates with ZAP-70 and Syk explain the impairment of β-selection in $RhoH^{-/-}$ mice. Considering the fact that Syk is critical in B cell development and BCR-dependent activation of B cells (41, 42), it is surprising that $RhoH^{-/-}$ mice showed normal B cell development and activation (data not shown). It is possible that B cells have another molecule having similar functions to RhoH, or the requirement for recruiting Syk to the membrane proximal could be different between BCR- and FcεRI-dependent signal transduction.

RhoH was reported to inhibit SDF-dependent activation of Rac1 in hematopoietic progenitor cells, and this was probably due to the inhibition of membrane targeting of Rac1 by RhoH (43). Therefore, the activity of Rac1 could be increased in the absence of RhoH. Indeed, Dorn et al. (6) showed that the PAK-binding activity of Rac1 in $RhoH^{-/-}$ T cells was increased without TCR stimulation. We did not observe enhanced phosphorylation of p38, a major downstream molecule of Rac1 in the absence or presence of FcεRI stimulation in $RhoH^{-/-}$ BMMCs (Fig. 5*D*), indicating that Rac1 is not over-activated in $RhoH^{-/-}$ mast cells. Precise function of RhoH on Rac1 regulation in mast cells should be elucidated in further studies.

Two independent groups have reported phenotypes of RhoH knockout mice (6, 7), and both of them showed defective T cell development and activation. Although both groups reported impaired phosphorylation of LAT (Y195) upon TCR stimulation, there is a discrepancy in the phosphorylation status of ZAP-70 (Y319) between the two groups. Dorn et al. (6) reported unaltered phosphorylation of ZAP-70, whereas Gu et al. (7) showed severely impaired ZAP-70 phosphorylation. Consequently, the former group hypothesized that RhoH is important for interaction between activated ZAP-70 and its substrate LAT, whereas the latter group hypothesized that RhoH is important for recruiting ZAP-70 to membrane proximal before activation. We observed impaired Syk activation upon FcεRI stimulation, evaluated by phosphorylation of Y519/520 in $RhoH^{-/-}$ mast cells (Fig. 6*A*), therefore, our results in mast cells are more consistent with the latter model in T cells. We also showed that RhoH and Syk can associate with each other without stimulation albeit very weakly, and the association was greatly enhanced by activation (Fig. 6*B*). From these results, we hypothesize that phosphorylated RhoH can associate strongly with Syk to keep Syk molecules at membrane proximal, thus facilitating effective activation of Syk. We tried to prove RhoH-dependent Syk recruitment by immunoprecipitaion and membrane subfractionation experiments. However, we were unable to detect membrane recruited Syk, possibly due to the fact that it is such a small proportion of total Syk (44). Future studies should clarify the function of RhoH in the recruitment of endogenous Syk in mast cells.

In the present study, we demonstrated that RhoH plays an important role in FcεRI-mediated activation of mast cells. RhoH$^{-/-}$ mice exhibited reduced systemic anaphylaxis in vivo, and RhoH$^{-/-}$ mast cells failed to degranulate and produce cytokines upon FcεRI stimulation in vitro. Because FcεRI-induced activation of Syk is dependent on RhoH, downstream events including phosphorylation of LAT, PLCγ1 and 2, and SLP-76 as well as Ca^{2+} mobilization in mast cells were all dependent on RhoH. RhoH associated with Syk when exogenously introduced, therefore it is possible that RhoH functions as an adaptor for Syk in mast cells, in a way analogous to its interaction with ZAP-70 in T cells (7). Collectively, these results indicate that RhoH positively regulates FcεRI signal transduction in mast cells. Because Syk is expressed in many kinds of hematopoietic lineage cells and involved in various ITAM-mediated signal transduction pathways (45), our current finding that RhoH facilitates Syk activation will shed new light on ITAM-based immune responses.

Acknowledgments

We thank Drs. S. Yamasaki, A. Yuo, T. Dohi, and S. Kano for technical instructions.

Disclosures

The authors have no financial conflict of interest.

References

1. Dallery, E., S. Galiegue-Zouitina, M. Collyn-d'Hooghe, S. Quief, C. Denis, M. P. Hildebrand, D. Lantoine, C. Deweindt, H. Tilly, C. Bastard, et al. 1995. TTF, a gene encoding a novel small G protein, fuses to the lymphoma-associated LAZ3 gene by t(3;4) chromosomal translocation. *Oncogene* 10: 2171–2178.
2. Aspenstrom, P., A. Ruusala, and D. Pacholsky. 2007. Taking Rho GTPases to the next level: the cellular functions of atypical Rho GTPases. *Exp. Cell Res.* 313: 3673–3679.
3. Li, X., X. Bu, B. Lu, H. Avraham, R. A. Flavell, and B. Lim. 2002. The hematopoiesis-specific GTP-binding protein RhoH is GTPase deficient and modulates activities of other Rho GTPases by an inhibitory function. *Mol. Cell Biol.* 22: 1158–1171.
4. Gu, Y., A. C. Jasti, M. Jansen, and J. E. Siefring. 2005. RhoH, a hematopoietic-specific Rho GTPase, regulates proliferation, survival, migration, and engraftment of hematopoietic progenitor cells. *Blood* 105: 1467–1475.
5. Cherry, L. K., X. Li, P. Schwab, B. Lim, and L. B. Klickstein. 2004. RhoH is required to maintain the integrin LFA-1 in a nonadhesive state on lymphocytes. *Nat. Immunol.* 5: 961–967.
6. Dorn, T., U. Kuhn, G. Bungartz, S. Stiller, M. Bauer, J. Ellwart, T. Peters, K. Scharffetter-Kochanek, M. Semmrich, M. Laschinger, et al. 2007. RhoH is important for positive thymocyte selection and T-cell receptor signaling. *Blood* 109: 2346–2355.
7. Gu, Y., H. D. Chae, J. E. Siefring, A. C. Jasti, D. A. Hildeman, and D. A. Williams. 2006. RhoH GTPase recruits and activates Zap70 required for T cell receptor signaling and thymocyte development. *Nat. Immunol.* 7: 1182–1190.
8. Underhill, D. M., and H. S. Goodridge. 2007. The many faces of ITAMs. *Trends Immunol.* 28: 66–73.
9. Bischoff, S. C. 2007. Role of mast cells in allergic and non-allergic immune responses: comparison of human and murine data. *Nat. Rev. Immunol.* 7: 93–104.
10. Wedemeyer, J., M. Tsai, and S. J. Galli. 2000. Roles of mast cells and basophils in innate and acquired immunity. *Curr. Opin. Immunol.* 12: 624–631.
11. Garman, S. C., J. P. Kinet, and T. S. Jardetzky. 1999. The crystal structure of the human high-affinity IgE receptor (FcεRIα). *Annu. Rev. Immunol.* 17: 973–976.
12. Kinet, J. P. 1999. The high-affinity IgE receptor (FcεRI): from physiology to pathology. *Annu. Rev. Immunol.* 17: 931–972.
13. Siraganian, R. P. 2003. Mast cell signal transduction from the high-affinity IgE receptor. *Curr. Opin. Immunol.* 15: 639–646.
14. Kraft, S., and J. P. Kinet. 2007. New developments in FcεRI regulation, function and inhibition. *Nat. Rev. Immunol.* 7: 365–378.
15. Gilfillan, A. M., and C. Tkaczyk. 2006. Integrated signalling pathways for mast-cell activation. *Nat. Rev. Immunol.* 6: 218–230.
16. Costello, P. S., M. Turner, A. E. Walters, C. N. Cunningham, P. H. Bauer, J. Downward, and V. L. Tybulewicz. 1996. Critical role for the tyrosine kinase Syk in signalling through the high affinity IgE receptor of mast cells. *Oncogene* 13: 2595–2605.
17. Nishizumi, H., and T. Yamamoto. 1997. Impaired tyrosine phosphorylation and Ca^{2+} mobilization, but not degranulation, in lyn-deficient bone marrow-derived mast cells. *J. Immunol.* 158: 2350–2355.
18. Parravicini, V., M. Gadina, M. Kovarova, S. Odom, C. Gonzalez-Espinosa, Y. Furumoto, S. Saitoh, L. E. Samelson, J. J. O'Shea, and J. Rivera. 2002. Fyn kinase initiates complementary signals required for IgE-dependent mast cell degranulation. *Nat. Immunol.* 3: 741–748.
19. Siraganian, R. P., J. Zhang, K. Suzuki, and K. Sada. 2002. Protein tyrosine kinase Syk in mast cell signaling. *Mol. Immunol.* 38: 1229–1233.
20. Iwaki, S., J. Spicka, C. Tkaczyk, B. M. Jensen, Y. Furumoto, N. Charles, M. Kovarova, J. Rivera, V. Horejsi, D. D. Metcalfe, and A. M. Gilfillan. 2008. Kit- and FcεRI-induced differential phosphorylation of the transmembrane adaptor molecule NTAL/LAB/LAT2 allows flexibility in its scaffolding function in mast cells. *Cell Signal* 20: 195–205.
21. Rivera, J., R. Arudchandran, C. Gonzalez-Espinosa, T. S. Manetz, and S. Xirasagar. 2001. A perspective: regulation of IgE receptor-mediated mast cell responses by a LAT-organized plasma membrane-localized signaling complex. *Int. Arch. Allergy Immunol.* 124: 137–141.
22. Singer, A. L., and G. A. Koretzky. 2002. Control of T cell function by positive and negative regulators. *Science* 296: 1639–1640.
23. Murata, T., K. Furushima, M. Hirano, H. Kiyonari, M. Nakamura, Y. Suda, and S. Aizawa. 2004. ang is a novel gene expressed in early neuroectoderm, but its null mutant exhibits no obvious phenotype. *Gene Expr. Patterns* 5: 171–178.
24. Yagi, T., T. Tokunaga, Y. Furuta, S. Nada, M. Yoshida, T. Tsukada, Y. Saga, N. Takeda, Y. Ikawa, and S. Aizawa. 1993. A novel ES cell line, TT2, with high germline-differentiating potency. *Anal. Biochem.* 214: 70–76.
25. Yamasaki, S., E. Ishikawa, M. Kohno, and T. Saito. 2004. The quantity and duration of FcRγ signals determine mast cell degranulation and survival. *Blood* 103: 3093–3101.
26. Plaut, M., J. H. Pierce, C. J. Watson, J. Hanley-Hyde, R. P. Nordan, and W. E. Paul. 1989. Mast cell lines produce lymphokines in response to cross-linkage of FcεRI or to calcium ionophores. *Nature* 339: 64–67.
27. Eiseman, E., and J. B. Bolen. 1992. Engagement of the high-affinity IgE receptor activates src protein-related tyrosine kinases. *Nature* 355: 78–80.
28. Millard, P. J., T. A. Ryan, W. W. Webb, and C. Fewtrell. 1989. Immunoglobulin E receptor cross-linking induces oscillations in intracellular free ionized calcium in individual tumor mast cells. *J. Biol. Chem.* 264: 19730–19739.
29. Koretzky, G. A., F. Abtahian, and M. A. Silverman. 2006. SLP76 and SLP65: complex regulation of signalling in lymphocytes and beyond. *Nat. Rev. Immunol.* 6: 67–78.
30. Nadler, M. J., S. A. Matthews, H. Turner, and J. P. Kinet. 2000. Signal transduction by the high-affinity immunoglobulin E receptor FcεRI: coupling form to function. *Adv. Immunol.* 76: 325–355.
31. Marshall, J. S. 2004. Mast-cell responses to pathogens. *Nat. Rev. Immunol.* 4: 787–799.
32. Abraham, S. N., and R. Malaviya. 1997. Mast cells in infection and immunology. *Infect. Immun.* 65: 3501–3508.
33. Hide, I., J. P. Bennett, A. Pizzey, G. Boonen, D. Bar-Sagi, B. D. Gomperts, and P. E. Tatham. 1993. Degranulation of individual mast cells in response to Ca^{2+} and guanine nucleotides: an all-or-none event. *J. Cell Biol.* 123: 585–593.
34. Saitoh, S., R. Arudchandran, T. S. Manetz, W. Zhang, C. L. Sommers, P. E. Love, J. Rivera, and L. E. Samelson. 2000. LAT is essential for FcεRI-mediated mast cell activation. *Immunity* 12: 525–535.
35. Pivniouk, V. I., T. R. Martin, J. M. Lu-Kuo, H. R. Katz, H. C. Oettgen, and R. S. Geha. 1999. SLP-76 deficiency impairs signaling via the high-affinity IgE receptor in mast cells. *J. Clin. Invest.* 103: 1737–1743.
36. Wu, J. N., M. S. Jordan, M. A. Silverman, E. J. Peterson, and G. A. Koretzky. 2004. Differential requirement for adapter proteins Src homology 2 domain-containing leukocyte phosphoprotein of 76 kDa and adhesion- and degranulation-promoting adapter protein in FcεRI signaling and mast cell function. *J. Immunol.* 172: 6768–6774.
37. Setoguchi, R., T. Kinashi, H. Sagara, K. Hirosawa, and K. Takatsu. 1998. Defective degranulation and calcium mobilization of bone-marrow derived mast cells from Xid and Btk-deficient mice. *Immunol. Lett.* 64: 109–118.
38. Kawakami, Y., J. Kitaura, A. B. Satterthwaite, R. M. Kato, K. Asai, S. E. Hartman, M. Maeda-Yamamoto, C. A. Lowell, D. J. Rawlings, O. N. Witte, and T. Kawakami. 2000. Redundant and opposing functions of two tyrosine kinases, Btk and Lyn, in mast cell activation. *J. Immunol.* 165: 1210–1219.
39. Negishi, I., N. Motoyama, K. Nakayama, K. Nakayama, S. Senju, S. Hatakeyama, Q. Zhang, A. C. Chan, and D. Y. Loh. 1995. Essential role for ZAP-70 in both positive and negative selection of thymocytes. *Nature* 376: 435–438.
40. Cheng, A. M., I. Negishi, S. J. Anderson, A. C. Chan, J. Bolen, D. Y. Loh, and T. Pawson. 1997. The Syk and ZAP-70 SH2-containing tyrosine kinases are implicated in pre-T cell receptor signaling. *Proc. Natl. Acad. Sci. USA* 94: 9797–9801.
41. Cheng, A. M., B. Rowley, W. Pao, A. Hayday, J. B. Bolen, and T. Pawson. 1995. Syk tyrosine kinase required for mouse viability and B-cell development. *Nature* 378: 303–306.
42. Turner, M., P. J. Mee, P. S. Costello, O. Williams, A. A. Price, L. P. Duddy, M. T. Furlong, R. L. Geahlen, and V. L. Tybulewicz. 1995. Perinatal lethality and blocked B-cell development in mice lacking the tyrosine kinase Syk. *Nature* 378: 298–302.
43. Chae, H. D., K. E. Lee, D. A. Williams, and Y. Gu. 2007. Cross-talk between RhoH and Rac1 in regulation of actin cytoskeleton and chemotaxis of hematopoietic progenitor cells. *Blood* 111: 2597–2605.
44. Wilson, B. S., J. R. Pfeiffer, Z. Surviladze, E. A. Gaudet, and J. M. Oliver. 2001. High resolution mapping of mast cell membranes reveals primary and secondary domains of FcεRI and LAT. *J. Cell Biol.* 154: 645–658.
45. Humphrey, M. B., L. L. Lanier, and M. C. Nakamura. 2005. Role of ITAM-containing adapter proteins and their receptors in the immune system and bone. *Immunol. Rev.* 208: 50–65.

Systemic Delivery of Synthetic MicroRNA-16 Inhibits the Growth of Metastatic Prostate Tumors via Downregulation of Multiple Cell-cycle Genes

Fumitaka Takeshita[1], Lubna Patrawala[2,3], Mitsuhiko Osaki[1,4], Ryou-u Takahashi[1], Yusuke Yamamoto[1,5], Nobuyoshi Kosaka[1], Masaki Kawamata[1], Kevin Kelnar[2,3], Andreas G. Bader[2,3], David Brown[2,3] and Takahiro Ochiya[1]

[1]*Section for Studies on Metastasis, National Cancer Center Research Institute, Tokyo, Japan;* [2]*Asuragen, Inc., Austin, Texas, USA;* [3]*Mirna Therapeutics, Inc., Austin, Texas, USA;* [4]*Division of Molecular Genetics and Biofunction, Tottori University Graduate School of Medical Science, Tottori, Japan;* [5]*Department of Biology, School of Education, Waseda University, Tokyo, Japan*

Recent reports have linked the expression of specific microRNAs (miRNAs) with tumorigenesis and metastasis. Here, we show that microRNA (miR)-16, which is expressed at lower levels in prostate cancer cells, affects the proliferation of human prostate cancer cell lines both *in vitro* and *in vivo*. Transient transfection with synthetic miR-16 significantly reduced cell proliferation of 22Rv1, Du145, PPC-1, and PC-3M-luc cells. A prostate cancer xenograft model revealed that atelocollagen could efficiently deliver synthetic miR-16 to tumor cells on bone tissues in mice when injected into tail veins. In the therapeutic bone metastasis model, injection of miR-16 with atelocollagen via tail vein significantly inhibited the growth of prostate tumors in bone. Cell model studies indicate that miR-16 likely suppresses prostate tumor growth by regulating the expression of genes such as *CDK1* and *CDK2* associated with cell-cycle control and cellular proliferation. There is a trend toward lower miR-16 expression in human prostate tumors versus normal prostate tissues. Thus, this study indicates the therapeutic potential of miRNA in an animal model of cancer metastasis with systemic miRNA injection and suggest that systemic delivery of miR-16 could be used to treat patients with advanced prostate cancer.

Received 21 May 2009; accepted 12 August 2009; published online 8 September 2009. doi:10.1038/mt.2009.207

INTRODUCTION

Advanced prostate cancer is frequently difficult to treat and causes substantial symptoms, including severe pain from metastasis to bone or other sites. Numerous experimental therapeutics are being pursued in clinical trials and offer some hope of improved treatments, but most have so far demonstrated only modest results.

Mounting evidence suggests that the altered expression of specific microRNA's (miRNA's) accuracy contributes to the development of a variety of cancers. Cancer types including prostate cancers can be classified based on their distinct miRNA expression profiles.[1–5]

MiRNAs have been implicated in prostate cancer. Volinia *et al.* identified >40 miRNAs with expression levels that were significantly different in prostate tumors versus normal prostate tissue.[5] Furthermore, the need for additional therapies in metastasis due to hormone-refractory prostate cancer is considerable. Mattie *et al.* found that miRNA expression in human prostate cancer cell lines could distinguish androgen hormone–insensitive PC3 from hormone-sensitive LNCaP cells.[6] LNCaP cells showed upregulation of microRNA (miR)-200c, miR-195, and several let-7 family members, whereas miR-10a, miR-27b, miR-221, miR-222, and mir-210 were lower than in PC3. The serum prostate-specific antigen is the most useful tumor marker for diagnosis and monitoring of prostate cancer. However, its low specificity in distinguishing prostate carcinoma from benign prostatic hyperplasia limits its use as an early detection biomarker. Investigators used custom designed arrays to compare the expression profiles of 319 miRNAs in prostate tumors, cancer cell lines, xenografts, and benign prostatic hyperplasia.[7] MiRNAs could be used to cluster the androgen receptor status of cell lines and xenografts. Among a small set of benign prostatic hyperplasia, hormone refractory, and untreated prostate carcinomas they found 51 differentially expressed miRNAs, 37 of which were downregulated. MiRNAs in this set accurately clustered the benign prostatic hyperplasia, untreated and hormone-refractory prostate carcinomas providing evidence that miRNA expression profiles are altered by changes in disease status. More recently, Bonci *et al.* showed that miR-15a and miR-16-1 cluster inhibit the tumor cell proliferation and invasion via targets CCND1 (cyclinD1), WNT3A, and BCL2 in prostate cancer cell line and clinical samples.[8] These miR-15a and miR-16-1 were coded on chromosome 9 13q14. In this region, loss of heterogeneity was detected in chronic lymphocytic leukemia[9] and prostate cancer patients.[10] These results suggest that miR-15a and/or miR-16 could be a novel target for prostate cancer therapy.

To supplement the expression studies that have been published for prostate cancer, we used a library of synthetic miRNAs

Correspondence: Takahiro Ochiya, Section for Studies on Metastasis, National Cancer Center Research Institute, 1-1, Tsukiji 5-chome, Chuo-ku, Tokyo 104-0045, Japan. E-mail: tochiya@ncc.go.jp

to identify the small RNAs that alter the proliferation of prostate cancer cells. Among the miRNAs that were identified in a functional screen featuring 22Rv1 prostate cancer cells was miR-16, an miRNA that has been implicated in chronic lymphocytic leukemia[1,11,12] and prostate cancer.[8,10] Our studies of miR-16 revealed that it has the capacity to affect the proliferation of a variety of human-derived prostate cancer cells. For the evaluation of miRNA therapy for bone metastasis of prostate cancer, the mouse model of bone-metastatic prostate cancer using bioluminescence-based *in vivo* imaging analysis was selected. We have already established small-interfering RNA (siRNA) molecules that can be delivered to tumor cells in a bone metastatic site using an atelocollagen delivery method.[13] The properties of synthetic miRNA molecules are similar to synthetic siRNA; therefore, it is speculated that synthetic miRNA can also be used for systemic treatment mediated by atelocollagen. In this article, the systemic delivery of synthetic miR-16 using atelocollagen inhibited bone-metastatic human prostate tumor growth in a mouse bone site. We further analyzed the altered expression of cancer-related genes in miR-16-transfected prostate cancer cells and verified that genes associated with cell-cycle progression were mostly affected by miR-16. These results suggest a therapeutic potency of miR-16 in bone-metastatic prostate cancer.

RESULTS

Effect of miR-16 on proliferation of human prostate cancer cell lines

22Rv1 prostate cancer cells were transiently transfected in triplicate with individual synthetic mimics for ~200 miRNAs. Three days after transfection, the cells were monitored for proliferation and apoptotic activity. Among the most active miRNAs identified in the functional screen was miR-16, which reduced the proliferation of the prostate cancer cells by 25% and increased apoptosis by 40% (data not shown). Follow-up studies for measuring the proliferation; using the alamar blue assay with another prostate cancer cell line, PC-3M-luc, revealed that miR-16 reduces proliferation by 60% (Figure 1a) relative to the cells transfected with a negative control (NC) miRNA. Further studies of the antiproliferative effect of miR-16 on prostate cancer cells revealed that synthetic miRNA can significantly affect the expansion of cultured 22Rv1, PPC-1, and Du145 cells (Figure 1a). The only prostate cancer cell line that proved to be unaffected by the transfection of miR-16 was LNCaP (Figure 1a). The amount of miR-16 in the PC-3M-luc cells transfected with synthetic miR-16 was >500-fold higher than that in the control cells (Figure 1b). This result suggests that the induced increase of intracellular miR-16 concentrations is capable of suppressing the proliferation of the prostate cancer cells.

miR-16 expression levels in prostate cancer cell lines

Although four of the five prostate cancer cell lines exhibit significant reductions in proliferation following transfection with synthetic miR-16, it is interesting that there is a variation in the level of the effect. To address whether this might be due to variation in the levels of endogenous miR-16 in the various cell lines, we used quantitative reverse transcription (qRT)-PCR to measure the relative abundance of mature miRNA. As shown in Figure 1c, most of the cell lines expressed miR-16 at reduced levels. The extent

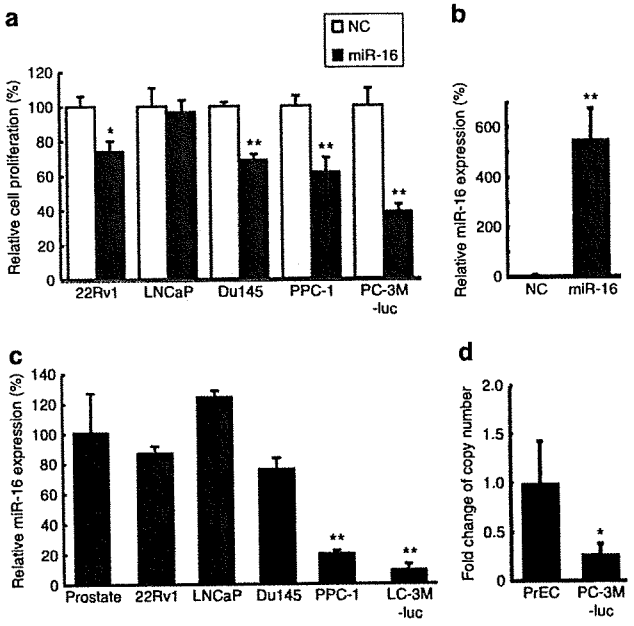

Figure 1 The expression and function of miR-16 in human prostate cancer cell lines. **(a)** Effect of miR-16 on proliferation of human prostate cancer cell lines. Percent (%) proliferation values were normalized to values from cells treated with negative control (NC) microRNA (miRNA). Data represent the mean ($n = 4$) ± SD $^*P < 0.05$, $^{**}P < 0.01$ versus NC miRNA. **(b)** The amount of miR-16 in PC-3M-luc cells transfected with synthetic miR-16. The cellular level of miR-16 was detected by quantitative PCR. The data represent the mean ($n = 3$) ± SD $^{**}P < 0.01$ versus NC miRNA. **(c)** Expression level of miR-16 in human prostate cancer cell lines. The relative expression of miR-16 for each of the cell lines was calculated by comparing the level in normal prostate tissue samples. The data represent the mean ($n = 3$) ± SD $^{**}P < 0.01$ versus normal human prostate tissue. **(d)** The copy number change of the miR-16 loci on chromosome 13q14 in PC-3M-luc cells. The copy number of miR-16 genes were quantified by real-time PCR with genomic DNA. Cultured normal human prostate epithelial cells (PrEC) was used as the control for this experiment for comparison to the PC-3M-luc cells. The data represent the mean ($n = 3$) ± SD $^*P < 0.05$ versus PrEC.

of downregulation correlated with the phenotypic response in these cell lines: *e.g.*, PPC-1 and PC-3M-luc cells, which showed the strongest response to miR-16, had the lowest levels of endogenous miR-16 (Figure 1a). The DNA copy numbers on chromosome 13q14, a genomic region that is frequently deleted in chronic lymphocytic leukemia and prostate cancer[14] in the PC-3M-luc cells were reduced to half that of normal prostate cells (Figure 1d). However, because the DNA sequence data did not show any mutations on chromosomes coding miR-16 of other copy in the PC-3M-luc cells (data not shown), the remarkable reduction of miR-16 expression might be invoked by a combination of DNA copy number alteration and other factors to affect the expression. LNCaP cells, which showed no response to the miR-16 mimic, were the only cells that tend to have higher miR-16 expression levels than the normal prostate (Figure 1c). Additionally, the transfection of miRNAs, which are not downregulated in PC-3M-luc cells, such as miR-10a and miR-188, did not inhibit the growth of PC-3M-luc cells (data not shown). The expression and function data suggest that reduced expression of miR-16 is critical for sustained proliferation in some prostate

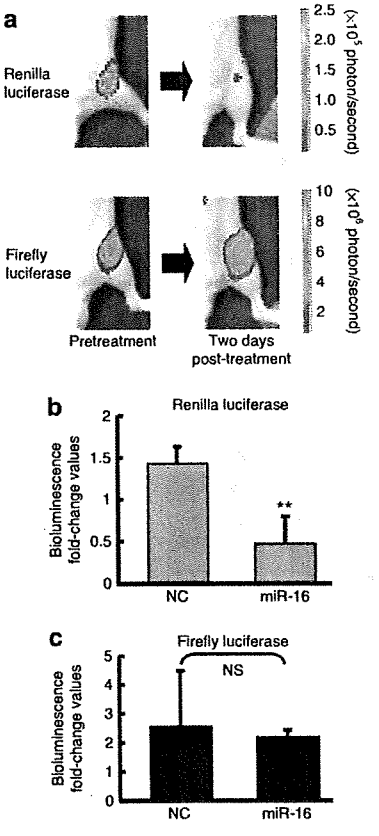

Figure 2 Evaluation of delivery for synthetic microRNA (miRNA) molecules to tumors in bone. A dual-luciferase expressing PC-3M cells that have 3′-UTR of Bcl2 under the renilla luciferase gene, PC-3M-luc/Rluc-Bcl2 3′UTR cells, were generated. These cells were used for dual assay system, for monitoring of tumor growth by firefly luciferase, for monitoring of delivery efficacy of synthetic miR-16 by renilla luciferase. **(a)** Representative images of bone metastasis in the femur of mice. To examine the efficacy of synthetic miR-16 in tumor cells, PC-3M-luc/Rluc-Bcl2 3′UTR cells were injected into the heart of nude mice. Nine weeks after tumor injection, bioluminescence from renilla luciferase was detected. Intravenous injection of miR-16 complexed with atelocollagen suppressed the expression of renilla luciferase (top). In contrast, bioluminescence from firefly luciferase was not affected (bottom). **(b)** Normalized fold change (2 days post/pre-miR-16 administration) of bioluminescence emitted from whole body of mice. This figure is graphically shown of the results of **Figure 2a** by fold change of photon counts. Data represent the mean (n = 3) ± SD *P < 0.01 versus NC miRNA. NS, not significant. NC, negative control.

cancer cell lines and that reintroduction of miR-16 can interfere with that phenotype.

Evaluation of miRNA delivery to bone-metastatic tumors in mice

In order to assess the capacity of the synthetic miR-16 to affect prostate tumor growth in mice, we chose to use a mouse model featuring PC-3M-luc cells that have the capacity to form prostate tumors in the bones of mice.[13,15,16] To evaluate that atelocollagen can efficiently deliver synthetic miRNA molecules to metastatic prostate tumors in bone, we generated a PC-3M-luc metastatic prostate cancer cell line stably expressing the renilla luciferase gene fused to the 3′UTR of Bcl2, a validated miR-16 target (**Supplementary Figure S1a**).[17] Thus, this newly engineered cell line PC-3M-Fluc/Rluc-Bcl2 3′UTR expresses both firefly and renilla luciferase, the later of which is under control of miR-16 (**Supplementary Figure S1b**). As expected, transfection of cultured PC-3M-Fluc/Rluc-Bcl2 3′UTR cells with 30 nmol/l of miR-16 deceased the luminescence derived from renilla luciferase (**Supplementary Figure S1c**). To monitor atelocollagen-mediated delivery of miR-16 in the animal, PC-3M-luc/Rluc-Bcl2 3′UTR cells were intracardiac injected into mice and allowed the tumor cells to deposit in the bone. Nine weeks after implantation, the mice were tail-vein injected with 50 μg of miR-16 mimic that was complexed with atelocollagen. Mice injected with the miR-16/atelocollagen complex produced <50% renilla luciferase from tumors in the bone than they produced before treatment (Figure 2a,b). The signal from the firefly luciferase that represents tumor growth was unaffected by the synthetic miR-16, indicating that the inhibition observed for renilla luciferase was due to the binding of injected synthetic miR-16 to the 3′UTR of Bcl2. Synthetic miR-16 was detected in tumor tissue at >20 pg/mg tissue when injected systemically and it was observed to persist in tumors for 3 days after injection (data not shown). Thus, our dual-luciferase prostate cancer xenograft model clearly showed that atelocollagen can efficiently deliver active miRNAs into metastatic tumors in mice.

Inhibition of tumor growth in bone tissues in mice with systemic miR-16 treatment

To assess the therapeutic potential of the miR-16/atelcollagen complexes, prostate tumors were initiated in the bones of mice by intracardiac injection of PC-3M-luc cells. A 50 μg of miR-16 mimic complexed with atelocollagen was administered intravenously into mice at 4, 7, and 10 days after prostate tumor initiation (**Supplementary Figure S2**). The development of tumor in the bone was monitored *in vivo* by bioluminescent imaging. At the end of the experiment on day 28, mice treated with the NC miRNA/atelocollagen complex showed the presence of tumor in the thorax, jaws, and/or legs of mice frequently (Figure 3a). In contrast, the mice injected with miR-16/atelocollagen complex exhibited no increase in luminescence during the same observation period. There are significant differences between NC and miR-16 treatment groups on day 28 (P < 0.05) (Figure 3b). Histopathological analysis also revealed that growth of PC-3M-luc cells in the bone tissues of mice was significantly inhibited by the miR-16 treatment (Figure 3c). These data suggest that atelocollagen-mediated systemic delivery of miR-16 could be a novel strategy for inhibition of prostate tumor growth in the bone tissues.

miR-16 expression in human prostate tissues

We used qRT-PCR to quantify miR-16 levels in the tumors and normal adjacent tissues of seven prostate cancer patients as well as four additional prostate tumors. The relative expression level of miR-16 in each of the samples was calculated by comparing to the average normalized miR-16 levels in prostate samples from three normal donors. The average relative expression of miR-16 in the seven prostate normal adjacent samples was 95% with a standard deviation of 16% and the eleven prostate tumors was 73% with a standard deviation of 28% (Figure 4). There is a trend toward lower miR-16 expression in prostate tumors versus normal

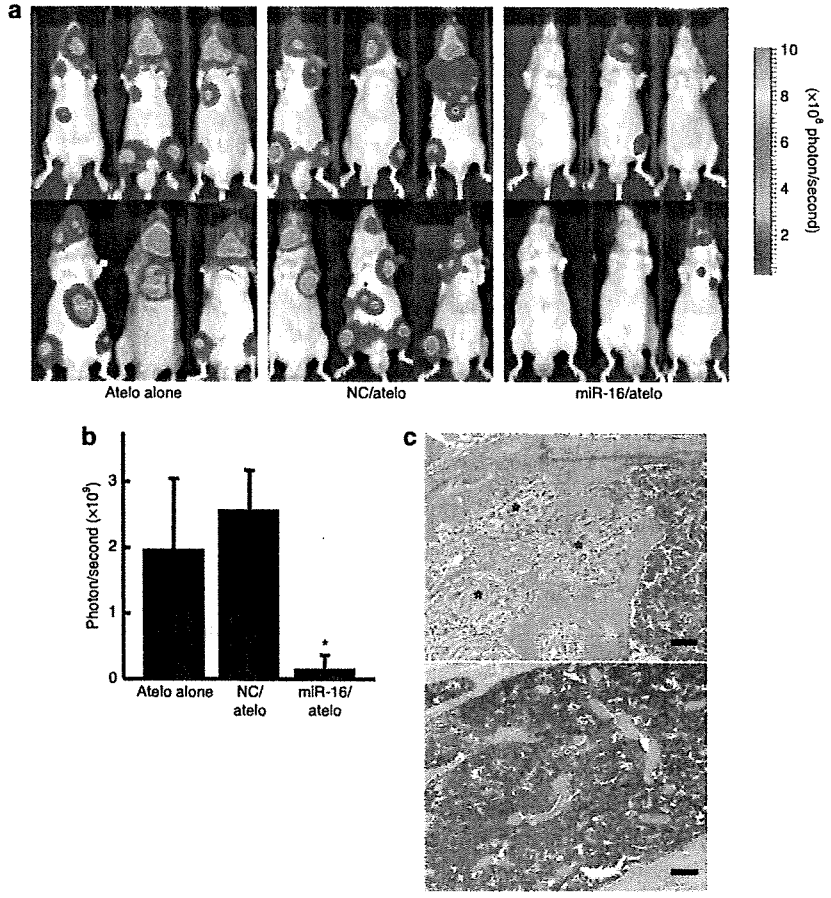

Figure 3 Inhibition of metastatic tumor growth in bone tissues by the atelocollagen-mediated miRNA treatment. Mice were injected with 2 × 10^6 PC-3M-luc-C6 cells into the left heart ventricle on day zero. The miR-16 and NC miRNA (50 µg) with 0.05% atelocollagen (Atelo) or Atelo alone in a 200 µl volume were injected into the tail vein on days 4, 7, and 10 after tumor injection. At the end of the experiment on day 28, the metastasis was evaluated by IVIS imaging and confirmed by subsequent necropsy. (**a**) All mice used in this experiment on day 28 were shown. There was an increase in luminescence in mice treated with atelocollagen alone and NC miRNA whereas the miR-16/atelocollagen-treated groups had no or low increase in luminescence during the same observation period. (**b**) Quantitation of bioluminescence emitted from whole body of mice on day 28. Data represent the mean (n = 6) ± SD *P<0.05 versus other groups. (**c**) Histopathological analysis confirmed micrometastasis in the tibia of nontreated mice (upper). Metastatic lesions are indicated by asterisk mark. In the miR-16-treated mice, any micrometastasis was not observed (lower). Bar = 100 µm.

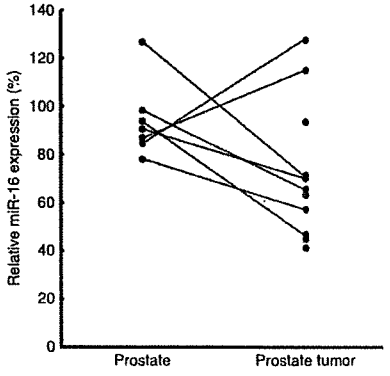

Figure 4 Clinical association of miR-16 expression with prostate cancer. The qRT-PCR analysis to quantify miR-16 levels in the tumors and normal adjacent tissues of seven prostate cancer patients and four additional prostate tumors was performed. The P value calculated by Student's t-test for the two sample sets was 0.08.

prostate tissues, but this trend did not reach statistical significance (Figure 4).

mRNA array analysis following transfection of synthetic miR-16

To get insight into the antioncogenic mechanism of miR-16, we transfected PC-3M-luc cells with the miR-16 mimic and analyzed the expressions of mRNA using mRNA array analysis. Exogenously, miR-16 might directly affect the mRNA levels of the target genes and indirectly affect the expression of genes that are downstream of these direct targets.[18] To identify the pathways that could be affected both directly and indirectly by miR-16, total RNA was isolated from the cells 72 hours after miR-16 transfection. The mRNA array data for the miR-16-transfected samples were compared to the NC miRNA–transfected samples (**Supplementary Table S1**). Fold-differential and P value calculations were used to select 285 mRNAs whose expression levels were significantly altered in the miR-16-transfected samples. A selection of genes suppressed

Table 1 Genes suppressed by miR-16

Gene title	Fold-change (miR-16 versus NC)[a]	*P* value[a]	Cellular process[b]
Aurora kinase B	0.61	2.83×10^{-5}	Chromosomal stability
BUB1	0.58	4.34×10^{-4}	Chromosomal stability
BUBR1	0.61	5.73×10^{-6}	Chromosomal stability
Cyclin D3	0.71	1.30×10^{-6}	Cell cycle
CDK1	0.58	4.99×10^{-7}	Cell cycle
CDK2	0.65	2.35×10^{-5}	Cell cycle
Double parked, DUP	0.76	4.07×10^{-5}	Chromosomal stability
Cks1	0.63	4.71×10^{-6}	Cell cycle
Forkhead box M1	0.61	8.19×10^{-6}	Transcription
Polo-like kinase 1	0.72	1.42×10^{-3}	Chromosomal stability
TACC1	0.76	1.56×10^{-4}	Cell cycle
TACC3	0.64	1.51×10^{-5}	Cell cycle
Thymidylate synthetase	0.56	2.50×10^{-8}	Nucleotide synthesis

Abbreviations: miRNA, microRNA; NC, negative control.
[a]Fold change and *P* value were determined by calculating the ratio of global normalized signals from miR-16 transfected cells to NC miRNA–transfected cells in expression array analysis. [b]Genes are clustered by cellular process, according to their gene ontology classification.

Table 2 Classes of genes affected by miR-16

Functional class	Count[a]	%[b]	*P* value[c]
M phase of mitotic cell cycle	20	12.7	9.60×10^{-18}
DNA metabolism	21	13.3	4.00×10^{-7}
Cytoskeleton organization and biogenesis	16	10.1	8.00×10^{-7}
Cytoskeleton-dependent intracellular transport	9	5.7	6.90×10^{-4}
Regulation of progression through cell cycle	15	9.5	2.50×10^{-5}
Mitotic sister chromatid segregation	4	2.5	6.10×10^{-4}
Establishment of cellular localization	13	8.2	4.10×10^{-3}
Mitotic spindle organization and biogenesis	3	1.9	5.50×10^{-3}
Regulation of progression through mitotic cell cycle	3	1.9	8.10×10^{-3}

[a]The number of genes affected in functional pathway. [b]The percentage calculated from the number of genes affected in functional pathway divided by the number of genes included on the arrays. [c]The significance of the appearance of the functional class in affected genes was calculated as *P* value using DAVID 2.0 software.

by miR-16 is listed in Table 1. Pathway analysis combining the Kyoto Encyclopedia of Genes and Genomes[19–21] and Database for Annotation, Visualization, and Integrated Discovery[22] was used to analyze the list of genes with altered expression to determine if there was a significant enrichment of genes associated with any known cellular pathways (Table 2). Overall, the statistical enrichment of pathways was moderately low, suggesting that no single pathway or network was specifically and vigorously responsive to the treatment. However, for those pathways that were considered enriched, a few strong underlying themes emerged. The gene lists were enriched for functions related to cell division and control of the cell cycle (Table 2). The functions associated with cell-cycle control were most enriched in miR-16-affected genes and these 12 genes that cover G1, S, G2, and M phase of cell cycle are mapped into the Kyoto Encyclopedia of Genes and Genomes Pathway Cell Cycle Map (**Supplementary Figure S3**). Thus, these data suggest that strong inhibition of prostate tumor growth in bone tissues of our animal model was due to downregulation of a key component of cell-cycle genes.

DISCUSSION

The likely involvement of miR-16 in the development of prostate cancer is apparent on multiple levels. The loss of the genomic locus at 13q14 that encompasses the miR-16-1 gene has been reported to be highly associated with human prostate cancer progression.[14] Dong *et al.* suggested loss of heterogeneity at 13q14 is associated with clinically significant high-grade and high-stage prostate cancers[10] with ties to both metastasis and tumor initiation.[23] Consistent with its genomic location, our qRT-PCR results showed that the miR-16 is significantly reduced in most prostate tumors and cultured prostate cancer cells relative to normal prostate tissues.

Based on our studies with cultured prostate cancer cells, the reduced expression of miR-16 is likely necessary to maintain high rates of proliferation. The relationship between miR-16 and apoptosis likely stems from the miRNA's apparent role in regulating BCL2 expression.[17] Our previous data also showed that the transfection of miR-16 into 22Rv1 prostate cancer cells induced apoptosis (F. Takeshita *et al.*, unpublished results). Although increased apoptosis is likely to be at least partially responsible for the reduced proliferation rates that we observed in miR-16-transfected PC-3M-luc cells, it appears that the small RNA also affects cell-cycle progression by regulating the expression of multiple cell-cycle genes. The transfection of prostate cancer cells with synthetic miR-16 reduced the expression of genes like *Cyclin D3*, *CDK1*, *CDK2*, *Cks1*, *TAAC1*, and *TAAC3* that play roles in regulating cell-cycle progression. The apparent capacity of miR-16 to simultaneously regulate cell cycle and apoptosis points to the likely importance of the small RNA in maintaining normal cell function and underscores the influence that the altered expression of the miRNA likely has on tumorigenesis.

The importance of miRNAs like miR-16 as tumor suppressors is becoming increasingly clear. Myriad array and qRT-PCR studies have revealed that the expression levels of specific miRNAs are reduced in the tumors of patients with a variety of cancers.[4,5] When transfected into cancer cells, many of these miRNAs affect proliferation, viability, cell cycle, or apoptosis[24,25] and affect the expression of multiple known oncogenes.[17,18,26–28] Although the growth inhibition of LNCaP cells was not induced by transfection of miR-16 in our study, Bonci *et al.* showed that such inhibition of LNCaP cells was induced by transduction of the *miR-15a-miR-16-1* cluster by lentiviral vector.[8] This discrepancy indicated that the growth inhibition of LNCaP might be induced mainly by induction of miR-15a, further careful studies are needed, considering any clinical application of miR-16.

The clinical application of these naturally occurring tumor suppressors represents a major opportunity for the future treatment

of cancer patients. As with other oligonucleotide-based therapies, realizing the potential of therapeutic miRNAs will require an effective delivery technology. In a previous study, we showed that intravenous injections of EZH2 and p110α siRNA complexed with atelocollagen inhibited the tumor growth in bone tissues of the mouse model.[13] These results showed that an atelocollagen-mediated systemic delivery of siRNA could reach tumor cells at metastatic sites and inhibit tumor growth *in vivo*. As demonstrated here, atelocollagen facilitates the accumulation of enough synthetic miRNA in the cancers cells of an existing prostate tumor to affect the expression of a target gene. Furthermore, the combination of synthetic miR-16 and atelocollagen strongly inhibited the development of human prostate tumors in the bones of mice. Interestingly, the effect of miR-16 appeared to be restricted to the prostate cancer cells, as the miR-16 treated mice showed no notable side effects. Follow-up studies featuring the treatment of larger tumors and more extensive toxicity studies will be required to demonstrate the therapeutic potential of atelocollagen-miR-16; however, these early results are extremely encouraging.

MATERIALS AND METHODS

Cell culture. The human prostate cell line 22Rv1, LNCaP, DU145, and PPC-1 cells were obtained from American Type Culture Collection (Manassas, VA) and maintained in RPMI 1640 medium containing 10% fetal bovine serum. The PC-3M-luc cells continuously expressing firefly luciferase (Xenogen, Alameda, CA) were maintained in RPMI 1640 medium supplemented with 10% fetal bovine serum and 0.2 mg/ml zeocin (Invitrogen, Carlsbad, CA). For construction of 3′-UTR–renilla luciferase plasmid and reporter assays, the segment of 3′-UTR of *Bcl2* gene was amplified by PCR using genomic DNA from normal human prostate epithelial cells (CT-2555; Lonza Walkersville, Walkersville, MD) as reported.[17] The PCR product was inserted into the pGL4.75[HRuc/CMV] vector (Promega, Madison, WI), using *XbaI* site immediately downstream from the stop codon of renilla luciferase (pGL4.75[HRuc/CMV]-Bcl2 3′UTR). For reporter assays, PC-3M-luc-C6 cells were transfected with 2 μg of pGL4.75[HRuc/CMV]-Bcl2 3′UTR using LipofectAMINE 2000 (Invitrogen). Stable transfectants were selected in hygromycine (0.2 mg/ml; Invitrogen) and bioluminescence was used to screen transfected clones for renilla and firefly luciferase gene expression using dual-luciferase assay system (Promega), intensity of renilla luciferase was normalized by firefly luciferase. Clones expressing the both luciferase gene were named PC-3M-luc/Rluc-Bcl2 3′UTR. The cells were maintained *in vitro* at 37 °C in a humidified atmosphere of 5% CO_2.

Transfection with synthetic miR-16 and assay of cellular proliferation. Synthetic hsa-miR-16 (Pre-miR-hsa-miR-16; Ambion, Austin, TX) or NC miRNA (Pre-miR microRNA Precursor Molecule-Negative Control #2, cat. no. AM17111; Ambion) was delivered via lipid-based reverse transfection with 30 nmol/l final concentration of miRNA as described previously.[29] As a control for inhibition of cellular proliferation, siRNA against the motor protein kinesin 11, also known as Eg5, was used. Eg5 is essential for cellular survival of most eukaryotic cells and a lack thereof leads to reduced cell proliferation and cell death.[30] siEg5 was used in lipid-based transfection following the same experimental parameters that apply to miRNA. We observed 50–70% growth inhibition in all cell lines used in this study. Percent (%) proliferation values from the alamar blue assay (Invitrogen) were normalized to values from cells treated with NC miRNA.

Quantitative RT-PCR of miR-16. Human cultured cell line RNA was isolated using the ISOGEN (Wako Chemical, Tokyo, Japan). MiRNA-specific complementary DNA was generated using the TaqMan MicroRNA RT Kit (Applied Biosystems, Foster City, CA) and the miRNA-specific RT primer from the TaqMan Micro RNA Assay (Applied Biosystems). The expression of the U6 small nuclear RNA was used as an internal normalization control. miRNA levels were also measured by using the miRNA-specific probe included with TaqMan Micro RNA Assay on a Real-Time PCR System 7300 and SDS software (Applied Biosystems).

Quantitative PCR of miR-16 loci on chromosome 13q14. Genomic DNAs were extracted from PC-3M-luc and prostate epithelial cells using DNAeasy (Qiagen, Valencia, CA). Quantitative PCR for the miR-16 loci on chromosome 13q14 was performed using Platinum SYBR Green qPCR SuperMix-UDG (Invitrogen) and primer sequences were 5′-GCA GCA CAG TTA ATA CTG GA-3′ and 5′-ATA GCT CTT ATG ATA GCA AT-3′. The house keeping gene, *RNase P* was also quantified as a control reference gene using Platinum Quantitative PCR SuperMix-UDG (Invitrogen) and TaqMan RNase P Detection Reagents Kit (Applied Biosystems). The reactions were incubated at 50 °C for 2 minutes, then heated to 95 °C for 2 minutes followed by 45 cycles of 15 seconds at 95 °C, and 30 seconds at 60 °C.

Evaluation of miRNA delivery to bone-metastatic tumors in mice. Animal experiments in this study were performed in compliance with the guidelines of the Institute for Laboratory Animal Research, National Cancer Center Research Institute. Seven- to ten-week-old male Balb/c athymic nude mice (CLEA Japan, Shizuoka, Japan) were anesthetized by exposure to 3% isoflurane on day zero and subsequent days. On day zero of the experiments, to generate a bone-metastatic human prostate cancer model, the anesthetized animals were injected with 2×10^6 PC-3M-luc/Rluc-Bcl2 3′UTR cells suspended in 100 μl sterile Dulbecco's phosphate-buffered saline into the left heart ventricle.[13,15,16] For *in vivo* imaging, the mice were injected with ViviRen (5 mg/kg; Promega) by intravenous tail vein injection and imaged immediately to count the photons from animal whole bodies using the IVIS imaging system (Xenogen). After the bioluminescence from renilla luciferase disappeared, photons from firefly luciferase were counted as described previously.[13]

Preparation of complex with miR-16 and atelocollagen. For preparing the complexes of miRNA and atelocollagen (Koken, Tokyo, Japan), an equal volume of atelocollagen (0.1 % in phosphate-buffered saline at pH 7.4) and miRNA solution were combined and mixed by rotating for 1 hour at 4 °C. The final concentration of atelocollagen was 0.05%. Nine weeks after tumor injection, individual mice (from cohorts containing three animals) were injected with 200 μl of atelocollagen containing 50 μg of miR-16 complexed with atelocollagen, or NC miRNA/atelocollagen by intravenous tail-vein injection.

Analysis of miR-16/atelocollagen treatment for bone-metastatic prostate cancer. Mice were inoculated with PC-3M-luc cells into the left cardiac ventricle on day zero as described previously.[13] The miR-16 and NC miRNA (50 μg) with 0.05% atelocollagen in a 200 μl volume were injected into the mouse tail vein on days 4, 7, and 10 postinoculation. Each experimental condition included six animals per group. At the end of the experiment on day 28, to confirm the presence of neoplastic cells, selected tissues were excised from the mice at necropsy. Tissues were fixed in 4% formaldehyde-phosphate-buffered saline(−), embedded in paraffin, cut into 5-μm sections, and stained with hematoxylin and eosin.

Clinical samples. Human prostate tissue samples derived from resected prostates from treatment-naive men with an average age of 65 (range of 52–76) diagnosed with nonmetastatic T2 or T3 prostate adenocarcinoma who gave informed consent. Gleason scores for all patients were 8 or 9. The tissues from patients were formalin-fixed, paraffin-embedded, sectioned, hematoxylin and eosin stained, and subjected to microscopic analysis. Three adjacent sections comprising 60–90% (74% average) cancerous tissue were selected as cancer samples from each patient. Three adjacent sections lacking evidence of cancer cells were selected as normal adjacent

samples. RNA from the tissues were prepared using the RecoverAll Total RNA Isolation Kit (Ambion). The isolated RNA was subjected to qRT-PCR for miR-16 as described above.

MiR-16 functional pathway analysis. For preparation of RNA samples, PC-3M-luc cells were reverse transfected in quadruplicate by complexing miR-16 and NC miRNA and NeoFX transfection reagent (Ambion). The final concentration of miRNA was 30 nmol/l. Cells were harvested at 72 hours post-transfection. One microgram of total RNA per sample was used to prepare biotin-labeled cRNA using a MessageAmp II-based protocol (Ambion) and one round of amplification. Labeled cRNA was hybridized, washed, and scanned using Illumina's recommended protocols. Illumina BeadScan software was used to produce .idat, .xml, and .tif files for each array on a slide. Raw data were extracted using Illumina BeadStudio software, v 3.0 (Illumina, San Diego, CA). Following quality assessment, data from the replicate beads on each array were summarized into average intensity values and variances. The background subtracted data were used to compare the relative expression of mRNAs in cells transfected with miR-16, NC miRNA, and transfection agent only. analysis of variance was used to judge the significance of the variation observed between the various treatment groups. In total, 285 mRNAs exceeded the thresholds used to identify differentially expressed genes (log ratio greater than 0.5 or less than −0.5 for the average signal between miR-16 and NC miRNA or transfection agent only treatments and P values <0.001 for the 72 hour time-point).

Statistical analysis. The results are given as mean ± SD Statistical analysis was conducted using the analysis of variance with the Bonferroni correction for multiple comparisons. A P value of ≤0.05 was considered to indicate a significant difference.

SUPPLEMENTARY MATERIAL

Figure S1. The scheme of dual luciferase assay for monitoring of systemic miR-16 delivery.

Figure S2. Overview of experimental protocol for inhibition of metastatic tumor growth in bone tissues by the atelocollagen-mediated miRNA treatment.

Figure S3. KEGG cell cycle diagram.

Table S1. Data of the mRNA array for comparison of miR-16 and NC miR transfected PC-3M-luc cells.

ACKNOWLEDGMENTS

We thank Ayako Inoue, Ayano Matsumoto, and Maho Kodama for their excellent technical work. We also thank Shunji Nagahara of Formulation Research Laboratories, Technology Research and Development Center, Dainippon Sumitomo Pharma Co., Ltd. for technological support and Koken Co., Ltd. for providing atelocollagen. This work was supported in part by a Grant-in-Aid for the Third-Term Comprehensive 10-Year Strategy for Cancer Control, a Grant-in-Aid for Scientific Research on Priority Areas Cancer from the Ministry of Education, Culture, Sports, Science and Technology, and the Program for Promotion of Fundamental Studies in Health Sciences of the National Institute of Biomedical Innovation (NiBio), and a Takeda Science Foundation.

REFERENCES

1. Calin, GA, Sevignani, C, Dumitru, CD, Hyslop, T, Noch, E, Yendamuri, S *et al.* (2004). Human microRNA genes are frequently located at fragile sites and genomic regions involved in cancers. *Proc Natl Acad Sci USA* **101**: 2999–3004.
2. Calin, GA, Ferracin, M, Cimmino, A, Di Leva, G, Shimizu, M, Wojcik, SE *et al.* (2005). A microRNA signature associated with prognosis and progression in chronic lymphocytic leukemia. *N Engl J Med* **353**: 1793–1801.
3. Calin, GA and Croce, CM (2006). MicroRNA-cancer connection: the beginning of a new tale. *Cancer Res* **66**: 7390–7394.
4. Lu, J, Getz, G, Miska, EA, Alvarez-Saavedra, E, Lamb, J, Peck, D *et al.* (2005). MicroRNA expression profiles classify human cancers. *Nature* **435**: 834–838.
5. Volinia, S, Calin, GA, Liu, CG, Ambs, S, Cimmino, A, Petrocca, F *et al.* (2006). A microRNA expression signature of human solid tumors defines cancer gene targets. *Proc Natl Acad Sci USA* **103**: 2257–2261.
6. Mattie, MD, Benz, CC, Bowers, J, Sensinger, K, Wong, L, Scott, GK *et al.* (2006). Optimized high-throughput microRNA expression profiling provides novel biomarker assessment of clinical prostate and breast cancer biopsies. *Mol Cancer* **5**: 24.
7. Porkka, KP, Pfeiffer, MJ, Waltering, KK, Vessella, RL, Tammela, TL and Visakorpi, T (2007). MicroRNA expression profiling in prostate cancer. *Cancer Res* **67**: 6130–6135.
8. Bonci, D, Coppola, V, Musumeci, M, Addario, A, Giuffrida, R, Memeo, L *et al.* (2008). The miR-15a-miR-16-1 cluster controls prostate cancer by targeting multiple oncogenic activities. *Nat Med* **14**: 1271–1277.
9. Bullrich, F and Croce, CM (2001). Molecular biology of chronic lymphocytic leukemia. In: Cheson, B (ed.). *Chronic Lymphoid Leukemia.* Dekker: New York, pp. 9–32.
10. Dong, JT, Boyd, JC and Frierson, HF (2001). Loss of heterozygosity at 13q14 and 13q21 in high grade, high stage prostate cancer. *Prostate* **49**: 166–171.
11. Calin, GA, Dumitru, CD, Shimizu, M, Bichi, R, Zupo, S, Noch, E *et al.* (2002). Frequent deletions and down-regulation of micro-RNA genes miR15 and miR16 at 13q14 in chronic lymphocytic leukemia. *Proc Natl Acad Sci USA* **99**: 15524–15529.
12. Calin, GA and Croce, CM (2006). Genomics of chronic lymphocytic leukemia microRNAs as new players with clinical significance. *Semin Oncol* **33**: 167–173.
13. Takeshita, F, Minakuchi, Y, Nagahara, S, Honma, K, Sasaki, H, Hirai, K *et al.* (2005). Efficient delivery of small interfering RNA to bone-metastatic tumors by using atelocollagen *in vivo*. *Proc Natl Acad Sci USA* **102**: 12177–12182.
14. Yin, Z, Spitz, MR, Babaian, RJ, Strom, SS, Troncoso, P and Kagan, J (1999). Limiting the location of a putative human prostate cancer tumor suppressor gene at chromosome 13q14.3. *Oncogene* **18**: 7576–7583.
15. Arguello, F, Furlanetto, RW, Baggs, RB, Graves, BT, Harwell, SE, Cohen, HJ *et al.* (1992). Incidence and distribution of experimental metastases in mutant mice with defective organ microenvironments (genotypes Sl/Sld and W/Wv). *Cancer Res* **52**: 2304–2309.
16. Jenkins, DE, Yu, SF, Hornig, YS, Purchio, T and Contag, PR (2003). *In vivo* monitoring of tumor relapse and metastasis using bioluminescent PC-3M-luc-C6 cells in murine models of human prostate cancer. *Clin Exp Metastasis* **20**: 745–756.
17. Cimmino, A, Calin, GA, Fabbri, M, Iorio, MV, Ferracin, M, Shimizu, M *et al.* (2005). miR-15 and miR-16 induce apoptosis by targeting BCL2. *Proc Natl Acad Sci USA* **102**: 13944–13949.
18. Johnson, CD, Esquela-Kerscher, A, Stefani, G, Byrom, M, Kelnar, K, Ovcharenko, D *et al.* (2007). The let-7 microRNA represses cell proliferation pathways in human cells. *Cancer Res* **67**: 7713–7722.
19. Kanehisa, M, Araki, M, Goto, S, Hattori, M, Hirakawa, M, Itoh, M *et al.* (2008). KEGG for linking genomes to life and the environment. *Nucleic Acids Res* **36**(Database issue): D480–D484.
20. Kanehisa, M and Goto, S (2000). KEGG: Kyoto Encyclopedia of Genes and Genomes. *Nucleic Acids Res* **28**: 27–30.
21. Kanehisa, M, Goto, S, Hattori, M, Aoki-Kinoshita, KF, Itoh, M, Kawashima, S *et al.* (2006). From genomics to chemical genomics: new developments in KEGG. *Nucleic Acids Res* **34**(Database issue): D354–D357.
22. Dennis, G, Sherman, BT, Hosack, DA, Yang, J, Gao, W, Lane, HC *et al.* (2003). DAVID: Database for Annotation, Visualization, and Integrated Discovery. *Genome Biol* **4**: P3.
23. Lu, W, Takahashi, H, Furusato, M, Maekawa, S, Nakano, M, Meng, C *et al.* (2006). Allelotyping analysis at chromosome 13q of high-grade prostatic intraepithelial neoplasia and clinically insignificant and significant prostate cancers. *Prostate* **66**: 405–412.
24. Chan, JA, Krichevsky, AM and Kosik, KS (2005). MicroRNA-21 is an antiapoptotic factor in human glioblastoma cells. *Cancer Res* **65**: 6029–6033.
25. Cheng, AM, Byrom, MW, Shelton, J and Ford, LP (2005). Antisense inhibition of human miRNAs and indications for an involvement of miRNA in cell growth and apoptosis. *Nucleic Acids Res* **33**: 1290–1297.
26. Johnson, SM, Grosshans, H, Shingara, J, Byrom, M, Jarvis, R, Cheng, A *et al.* (2005). RAS is regulated by the let-7 microRNA family. *Cell* **120**: 635–647.
27. Lim, LP, Lau, NC, Garrett-Engele, P, Grimson, A, Schelter, JM, Castle, J *et al.* (2005). Microarray analysis shows that some microRNAs downregulate large numbers of target mRNAs. *Nature* **433**: 769–773.
28. Lewis, BP, Burge, CB and Bartel, DP (2005). Conserved seed pairing, often flanked by adenosines, indicates that thousands of human genes are microRNA targets. *Cell* **120**: 15–20.
29. Ovcharenko, D, Jarvis, R, Hunicke-Smith, S, Kelnar, K and Brown, D (2005). High-throughput RNAi screening *in vitro*: from cell lines to primary cells. *RNA* **11**: 985–993.
30. Weil, D, Garçon, L, Harper, M, Duménil, D, Dautry, F and Kress, M (2002). Targeting the kinesin Eg5 to monitor siRNA transfection in mammalian cells. *BioTechniques* **33**: 1244–1248.

THE JOURNAL OF GENE MEDICINE
J Gene Med 2009; **11**: 615–623.
Published online 27 April 2009 in Wiley InterScience (www.interscience.wiley.com) **DOI:** 10.1002/jgm.1338

RESEARCH ARTICLE

Intranuclear fluorescence resonance energy transfer analysis of plasmid DNA decondensation from nonviral gene carriers

Yu Matsumoto[1,2]
Keiji Itaka[1]
Tatsuya Yamasoba[2]
Kazunori Kataoka[1,3,4]*

[1]*Division of Clinical Biotechnology, Center for Disease Biology and Integrative Medicine, Graduate School of Medicine, The University of Tokyo, Tokyo, Japan*

[2]*Department of Otorhinolaryngology and Head and Neck Surgery, Graduate School of Medicine and Faculty of Medicine, The University of Tokyo, Tokyo, Japan*

[3]*Department of Materials Engineering, Graduate School of Engineering, The University of Tokyo, Tokyo, Japan*

[4]*Center for Nanobio Integration, The University of Tokyo, Tokyo, Japan*

*Correspondence to:
Kazunori Kataoka, Department of Materials Engineering, Graduate School of Engineering, The University of Tokyo, 7-3-1 Hongo, Bunkyo-ku, Tokyo 113-0033, Japan.
E-mail: kataoka@bmw.t.u-tokyo.ac.jp

Received: 21 January 2009
Revised: 23 March 2009
Accepted: 24 March 2009

Abstract

Background There has been considerable interest in researching the regulatory mechanisms that control transgene expression. In particular, there is impetus to investigate the intranuclear mechanisms for gene expression in order to improve the transfection efficiency of nonviral gene carriers.

Methods To clarify the direct relationship between DNA decondensation and gene expression, plasmid DNA encoding Keima-Red fluorescent protein was doubly-labeled by a pair of donor–acceptor fluorescent dyes (fluorescein and Cy3), and transfected to HuH-7 cells using nonviral gene carriers: polyethylenimine (polyplex) and LipofectAMINE 2000 (lipoplex). Fluorescence resonance energy transfer analysis between the two dyes represents the condensation state of the pDNA. The intranuclear trafficking and condensation state of the pDNA were explored in transgene expressing and non-expressing cells under confocal laser scanning spectromicroscopy.

Results The majority of transgene positively expressing cells transfected with polyplex and lipoplex had decondensed pixels in the nucleus. The majority of non-expressing cells transfected with polyplex had only condensed pixels in the nucleus. The majority of non-expressing cells transfected with lipoplex had no pixels in the nucleus.

Conclusions Both polyplex and lipoplex marked a strong correlation between pDNA decondensation and transgene expression, yet the major limiting factor for transgene expression was different. In polyplex, the pDNA decondensation after nuclear entry was the major determining factor for transgene expression, whereas the nuclear entry itself was the chief determining step for transgene expression by lipoplex. This imaging technique allowed *in situ* observation of pDNA in the nucleus, providing important information about DNA behavior for gene expression.

Keywords confocal microscopy; DNA decondensation; fluorescence resonance energy transfer; lipoplex; polyplex; transfection

Introduction

The gene delivery system plays a key role in achieving the therapeutic effect in successful gene therapy. Viral vectors such as adenoviral vectors are considered to be the most efficient gene delivery systems, but also

present many disadvantages, such as inflammatory and immunological reactions. Chemical delivery systems are highly potent and promising devices presenting an interesting alternative to viral vectors. The advantages of nonviral systems include low cytotoxicity, the lack of immunogenicity, large nucleic acid capacity and ease of production. However, sufficient transfection efficiency for clinical application has not been achieved [1]. Improvement of the transfection efficiency is one of the most important subjects for the development of nonviral gene delivery systems. Two major classes of nonviral vectors that have shown relatively high efficiency are cationic polymers and cationic lipids. It is well recognized that these nonviral gene carriers combine pDNA through electrostatic interaction. They form compact complexes (polyplexes, lipoplexes) and protect the DNA from enzymatic degradation. As a result of the excess cationic polymers or lipids, these carriers induce a positive charge at the complex surface, which is considered to facilitate the association with plasma membrane. There are many intracellular processes, such as endocytic internalization, trafficking in the cytoplasm, nucleus entry and transcription, which hamper gene carriers in achieving successful transfection. Among these processes, transcription in the nucleus is one of the major obstacles determining the transfection efficiency, although the exact mechanism is still largely unknown [2,3]. It is widely accepted that the lipoplexes should be disassociated before they are involved in transcription [4,5], but there is still controversy over whether the polyplexes should be completely disrupted before transcription [6–9].

We previously analysed the condensation status of plasmid DNA (pDNA) inside nonviral gene carriers by fluorescent resonance energy transfer (FRET) using double-labeled pDNA. The sensitive *in vitro* analysis of the nanoscale conformational change of pDNA in the physiological condition [10] was followed up by *in situ* observation of FRET inside the cells using a laser confocal microscope, demonstrating the close relationship between the condensation status of pDNA inside the cells and transgene expression [11].

To clarify the direct relationship between DNA decondensation and its transcriptional activity, we developed a novel imaging technique for fluorescent analysis using a confocal laser-scanning spectromicroscope to visualize the pDNA decondensation with fluorescent spectral data obtained from cell images. In addition, the transgene expression was evaluated using the fluorescent reporter gene. A fluorescent labeling technique of pDNA that remains its transgene expression competency [12] allowed us to investigate the structure–function relationship of the pDNA in every single cell. Through observation of the double-labeled pDNA encoding the Keima-Red reporter gene, the pDNA condensation state was analysed from the fluorescent spectral data, and the Keima-Red expression was simultaneously detected. Eventually, the status of pDNA condensation as a result of intracellular processes was revealed to be a crucial factor determining the transgene expression.

Materials and methods

Cell culture

Huh-7 cells were obtained from the Riken Cell Bank (Tsukuba, Japan). The cells were grown in Dulbecco's Modified Eagle's Medium (Sigma-Aldrich Corp., St Louis, MO, USA) supplemented with 50 μg/ml of penicillin/streptomycin and 10% (v/v) fetal bovine serum (FBS) in a 5% CO_2/air incubator at 37 °C. The cells were passed regularly once per week via trypsinization.

Preparation of pDNA

A pDNA-encoding CoralHue Monomeric Keima-Red fluorescent protein with CMV promoter (pmKeima-Red-MN1) was purchased from MBL (Woburn, MA, USA). A pDNA-encoding luciferase protein with a SV40 promoter (pGL4.13[luc2/SV40]) was purchased from Promega (Madison, WI, USA). Both pDNAs were amplified using *Escherichia coli* DH5α and purified with a NucleoBond Xtra Maxi kit (Macherey-Nagel, Düren, Germany). The purity and concentration of pDNA were confirmed by ultraviolet (UV) spectrophotometry at 260 nm and 280 nm using a NanoDrop ND-1000 UV-Vis Spectrophotometer (NanoDrop Technologies, Wilmington, DE, USA).

Fluorescent labeling of pDNA

pDNA was labeled using Label IT Tracker Intracellular Nucleic Acid Localization Kits (Mirus Bio Corporation, Madison, WI, USA). By this labeling method, the pDNA remains transgene expression competency, even after the covalent attachment of fluorophores [12]. Thus, both the subcellular localization of DNA and its transgene expression were monitored together in the same cell. The manufacturer's labeling protocol was slightly modified, using two labeling kits. Fluorescein (ex/em = 492/518) and Cy3 (550/570) kits were used for the donor–acceptor pair. Briefly, 1000 μl of pmKeima-Red-MN1 solution (1 mg/ml), 250 μl of Label IT Tracker Fluorescein reagent, and 250 μl of Label IT Tracker Cy3 reagent were mixed in 20 mM MOPS buffer (pH 7.5) and incubated at 37 °C for 1.5 h. For double-labeling with fluorescein and Cy3, two reagents were added simultaneously to the pDNA solution. After the incubation, unreacted reagents were removed by ethanol precipitation to purify the pDNA. To avoid the fluctuation caused by incorporating the two dyes between different labeling reactions, an adequate amount of pDNA for the entire study (1 mg) was labeled at a single preparation and kept separately in small quantities at −30 °C. At each experiment, the fluorescent emission spectrum of the stocked pDNA was measured to check the stability.

Transfection

Huh-7 cells were seeded at a density of 1×10^5 cells in 35-mm glass bottom dishes (Asahi Techno Glass Corporation, Chiba, Japan) precoated with type I-C collagen (Nitta Gelatin Inc., Osaka, Japan). After overnight incubation in medium containing 10% FBS, the cells were washed with PBS twice, and 2 ml of culture medium without FBS were added to each dish. ExGen 500 (Fermentas, Burlington, Canada) and LipofectAMINE 2000 (Invitrogen Corporation, Carlsbad, CA, USA) were used for transfection. The pDNA complexes were prepared following the manufacturers' instructions. According to preliminary experiments aiming to determine the ideal transfection condition, the nitrogen/pDNA phosphate (N/P) ratio of ExGen 500 and the pDNA (μg) to LipofectAMINE 2000 (μl) ratio were set at 10 and 1 : 0.67, respectively. After 1 h of transfection, the dishes were washed twice with PBS and replaced with complete medium to terminate the cellular uptake of pDNA complexes. Incubation was continued until the appropriate time for all time points of the observation. Fifteen minutes before each observation, Hoechst 33 342 (Dojindo, Kumamoto, Japan) was applied to the medium to stain the nucleus.

Fluorospectrometry

The spectral properties of the double-labeled pDNA/ExGEN 500 complex (polyplex) and pDNA/Lipofect-AMINE 2000 complex (lipoplex) were investigated along with free pDNA using a NanoDrop ND-3300 fluorospectrometer (NanoDrop Technologies) upon excitation at 470 nm by blue LED.

Confocal laser-scanning spectromicroscopy

All imaging of the cells was performed using a Zeiss 510 META nonlinear optics scan head attached to an inverted Axiovert 200 M SP equipped with a ×63, 1.4 numerical aperture planachromat water immersion objective (Carl Zeiss Inc., Jena, Germany). Using the standard photomultiplier detection channels, Hoechst 33 342 (ex/em = 352/468) and Keima-Red (ex/em = 440/620) signals were obtained along with a differential interference contrast (DIC) image. Five sequential 1-μm thick Z-sections were captured at all field angles, with a middle section set manually to yield the greatest dimension of the nucleus. To determine the intensity of fluorescein and Cy3, spectral imaging and subsequent linear unmixing were performed on the same five optical slices. Using 16 channels of the internal META detector, a spectral image (Lambda stack image) was obtained by 488 nm laser excitation (506–667 nm, spectral bandwidth per channel 10.7 nm) with the same five sequential Z-sections (Lambda-Z stack image). Pure fluorescein- and pure Cy3-labeled pGL4.13[luc2/SV40] were dispensed to obtain each reference spectrum and saved to the spectral database for the subsequent linear unmixing. A background spectrum, acquired from regions lacking fluorophores of the spectral image to be unmixed, was also saved to the database. Three reference spectra were used for linear unmixing: a fluorescein spectrum, a Cy3 spectrum, and a background spectrum. Lambda Z-stack images were unmixed into three respective channels. The fluorescein and Cy3 image channels were simply divided to calculate the F/C ratio for every fluorophore. A pixel-by-pixel calculation of the fluorescein/Cy3 (F/C) ratio was obtained by a simple arithmetic expression described below, adopting the 'Formula' menu of the Zeiss META software:

$$\text{SELECT (Cy3} > 50,\ \text{fluorescein/Cy3,0)}$$

where 'SELECT' is a pre-defined operator, which performs the second operant (Fluorescein/Cy3 calculation) upon the satisfaction of the first operant (Cy3 > 50), and responds with the third operant (0) otherwise. In this case, a Cy3 threshold of 50 was determined as the presence of fluorophores, and all other pixels were set to zero (black). Each pixel with a Cy3 value above 50 was qualified for ratio calculation, and the division of fluorescein/Cy3 was performed.

Exchange reaction between poly(aspartic acid) and pDNA in the polyplex

The pDNA release and decondensation from the polyplex were investigated by adding poly(aspartic acid) sodium salt (relative molecular mass = 26 000; Sigma-Aldrich Corp.). Twelve unit molar ratios of poly(aspartic acid) solutions ([carboxyl groups in poly(aspartic acid)]/[phosphate groups in pDNA]) were added and incubated at room temperature for 2 h, and the polyplex solutions were analysed with a fluorospectrometer. Pure fluorescein- and pure Cy3-labeled pDNA were also dispensed to obtain each reference spectrum, and the F/C ratio was calculated by mimicking the linear unmixing algorithm equipped in the Zeiss 510 META software.

Results

Fluorescent spectra obtained in buffer solution and on cell images

The condensation state of pDNA inside nonviral gene carriers was evaluated in 10 mM Tris-HCl (pH 7.4) solution by analysing the change in the spectral properties of the pDNA doubly-labeled with fluorescein and Cy3. After the complexation of pDNA with linear polyethylenimine (ExGen 500), the emission spectrum under excitation at 470 nm showed an increase in Cy3

DOI: 10.1002/jgm

intensity (560 nm) and a decrease in fluorescein intensity (517 nm) compared to free pDNA. After the complexation of pDNA with cationic lipid (LipofectAMINE 2000), the emission spectrum showed little change compared to free pDNA (Figure 1a).

The emission spectra of polyplexes and lipoplexes were analysed inside the cells by confocal laser-scanning spectromicroscopy. The spectrum obtained from the cell images was identical to that obtained in the buffer solution (Figure 1b). Each fluorescent pixel had their respective spectra for polyplexes (Figures 1b and 1c). Similar emission spectra were obtained from cell images after the transfection using lipoplex (data not shown).

In vitro analysis on DNA decondensation

After complexation with linear polyethylenimine (LPEI; Exgen 500) at N/P = 10 in 10 mM Tris-HCl (pH 7.4) solution, poly(aspartic acid) was added to the polyplex at 12 different unit molar ratios ([carboxyl groups in poly(aspartic acid)]/[phosphate groups in pDNA]). The F/C ratios were calculated from the spectra and plotted against respective unit molar ratios (Figure 2). At a unit molar ratio of zero, where no poly(aspartic acid) was added, the F/C ratio was 0.3. The F/C ratios were below 0.4 at unit molar ratios from zero to seven. The F/C ratio continuously increased as the unit molar ratios increased from eight, with a steep increase at the unit molar ratio from eight to 12, and a gradual increase at the unit molar ratio from 14 to 20. The F/C ratio was 2.5 at the unit molar ratio of 20. Note that the F/C ratio of the double-labeled free plasmid with no complexation was 2.8.

Transgene expression

No Keima-Red florescence signal was detected after 1 and 3 h after transfection. The Keima-Red fluorescence initially became detectable at 6 h after transfection. The fluorescence was determined using appropriate filter sets, and was confirmed by emission spectrum using a META detector. The fluorescent intensity of Keima-Red increased at 24 h after transfection. Both polyplex and lipoplex showed comparable transgene expression at either one or several days after transfection (data not shown).

Frequency histogram of F/C ratios

At 6 h after transfection, the condensation state of pDNA inside the nuclei of both the Keima-Red positive cells and negative cells were analysed (Figure 3). Keima-Red positive and negative cells were selected, respectively, and the F/C ratio of every fluorescent clump inside the nuclei was investigated. The frequency histogram of the F/C ratio was obtained (Figure 4). In both polyplex and lipoplex, the Keima-Red positive cells had pixels with F/C ratios ≥ 0.4, whereas Keima-Red negative cells had few if any pixels with F/C ratios ≥ 0.4. Irrespective of the F/C ratio (x-axis), the pixel counts on the y-axis in total were higher for polyplex than lipoplex.

Merged cell images

At 1, 3, and 6 h after transfection, the F/C ratios of pDNA were calculated (Figure 3). Pixels with F/C ratio ≥ 0.4 were colored green. Pixels with F/C ratios <0.4 were colored red. Both calculational images were merged onto Keima-Red cell images (Figure 5).

At 1 h after transfection using polyplex, both green and red clumps were observed in the plasma membrane, cytoplasm, and nucleus. The red clumps were larger than the green clumps (Figure 5a). Green and red pixels formed chimeral patterns in some large clumps. Using lipoplex, clumps were observed in the plasma membrane,

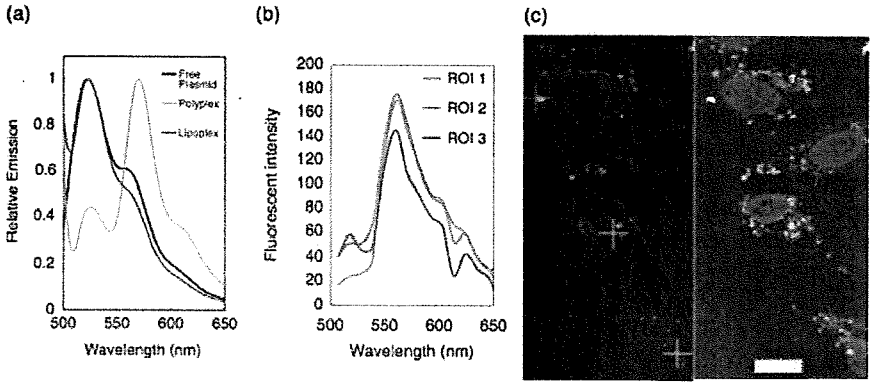

Figure 1. (a) The condensation state of pDNA inside the carriers was evaluated by analysing the change of the spectral properties of the pDNA doubly-labeled with fluorescein and Cy3. Spectral properties of double-labeled free pDNA, polyplexes and lipoplexes were investigated upon excitation at 470 nm. (b) Huh-7 cells were transfected with double-labeled pDNA using ExGen 500. Spectral images were obtained using the META detector by 488 nm laser excitation. Three typical fluorescent spectra are presented along with the corresponding spectral and DIC images (c). In this case, the region of interest (ROI) 1 has low fluorescein intensity and high Cy3 intensity, indicating that complex is still in a condensed state. The fluorescein intensity of ROI 2 or 3 is elevated, indicating that the complex has undergone partial decondensation. Scale bar = 20 μm

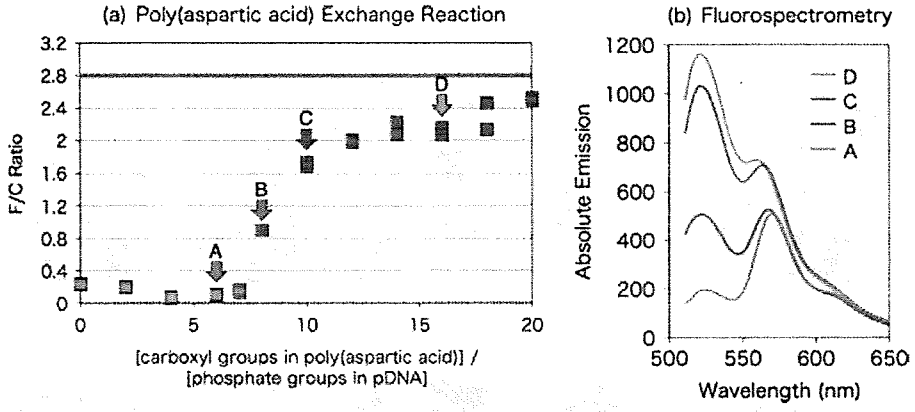

Figure 2. (a) Exchange reaction between poly(aspartic acid) and pDNA in the polyplex. Poly(aspartic acid) was added to the polyplex at 12 unit molar ratios ([carboxyl groups in poly(aspartic acid)]/[phosphate groups in pDNA]), and F/C ratios were calculated from the spectra obtained. F/C ratios were plotted against [carboxyl groups in poly(aspartic acid)]/[phosphate groups in pDNA] ratios. The left most (unit molar ratio = 0) is the F/C ratio of polyplex with no addition of poly(aspartic acid). The F/C ratio of the double-labeled free plasmid with no complexation was 2.8 (blue). (b) Representative spectra are shown for the indicated points in (a)

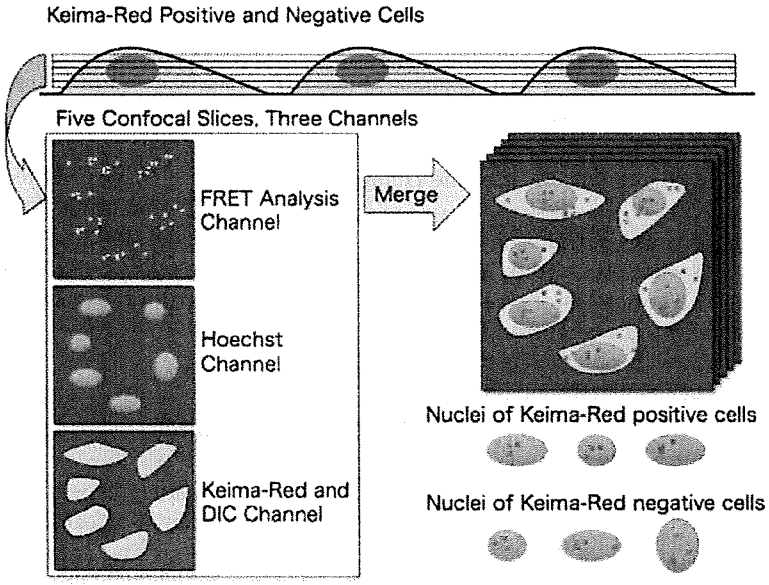

Figure 3. Schematic diagram of intranuclear FRET analysis. Cells were scanned to cover the entire thickness of the nucleus by five sequential confocal slices upon three different excitation channels. Pixel-to-pixel calculation of the F/C ratio was performed for the FRET analysis. Keima-Red positive and negative cells were selected, respectively, and the F/C ratio of every fluorescent clump inside the nuclei was investigated

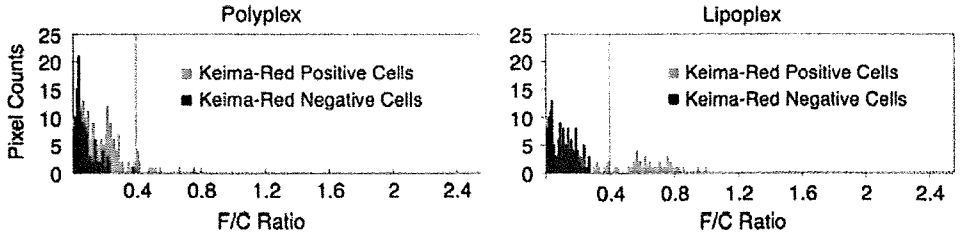

Figure 4. F/C ratio histogram of pixels inside the nucleus of Keima-Red positive and negative cells transfected with polyplex and lipoplex. Keima-Red positive cells had more clumps of high F/C ratios compared to the Keima-Red negative cells in both polyplex and lipoplex

DOI: 10.1002/jgm